Nonequilibrium kinetic freeze-out properties in relativistic heavy ion collisions from energies employed at the RHIC beam energy scan to those available at the LHC

Jia Chen [1,2] Jian Deng,[1,2] Zebo Tang,[3] Zhangbu Xu [4] and Li Yi [1,2,*]

[1]*Institute of Frontier and Interdisciplinary Science, Shandong University, Qingdao, Shandong 266237, China*

[2]*Key Laboratory of Particle Physics and Particle Irradiation of Ministry of Education, Shandong University, Qingdao, Shandong 266237, China*

[3]*State Key Laboratory of Particle Detection and Electronics, University of Science and Technology of China, Hefei, Anhui 230026, China*

[4]*Brookhaven National Laboratory, Upton, New York 11973, USA*

(Received 7 December 2020; revised 29 May 2021; accepted 2 August 2021; published 1 September 2021)

In this paper, we investigate the kinetic freeze-out properties in relativistic heavy ion collisions at different collision energies. We present a study of standard Boltzmann-Gibbs blast-wave (BGBW) fits and Tsallis blast-wave (TBW) fits performed on the transverse momentum spectra of identified hadrons produced in Au+Au collisions at collision energies of $\sqrt{s_{\rm NN}} = 7.7$–200 GeV at the Relativistic Heavy Ion Collider (RHIC), and in Pb+Pb collisions at collision energies of $\sqrt{s_{\rm NN}} = 2.76$ and 5.02 TeV at the Large Hadron Collider (LHC). The behavior of strange and multistrange particles is also investigated. We found that the TBW model describes data better than the BGBW one overall, and the contrast is more prominent as the collision energy increases as the degree of nonequilibrium of the produced system is found to increase. From TBW fits, the kinetic freeze-out temperature at the same centrality shows a weak dependence of collision energy between 7.7 and 39 GeV, while it decreases as collision energy continues to increase up to 5.02 TeV. The radial flow is found to be consistent with zero in peripheral collisions at RHIC energies but sizable at LHC energies and central collisions at all RHIC energies. We also observed that the strange hadrons, with higher temperature and similar radial flow, approach equilibrium more quickly from peripheral to central collisions than light hadrons. The dependence of temperature and flow velocity on nonequilibrium parameter $(q-1)$ is characterized by two second-order polynomials. Both a and $d\xi$ from the polynomials fit, related to the influence of the system bulk viscosity, increase toward lower RHIC energies.

DOI: 10.1103/PhysRevC.104.034901

I. INTRODUCTION

Relativistic heavy ion collisions can create extreme hot and dense matter and reach a phase transition to quark-gluon plasma (QGP). As QGP expands rapidly, its temperature drops and the system starts to enter the hadronic phase. Eventually the system reaches kinetic freeze-out when all particle interactions cease. The particle spectra are thus frozen, which carry information about system dynamics at that freeze-out and even earlier. Therefore, the study of differential transverse momentum (p_T) distributions of hadron particles is a useful tool to look into the evolution of the system, especially to extract system properties at its freeze-out phase space. The Boltzmann-Gibbs blast-wave (BGBW) model [1,2] has been widely used to describe the produced system at kinetic freeze-out with its systemwise parameters characterizing the system radial flow velocity and temperature.

The BGBW model assumes that the produced system has reached local thermal equilibrium so that a Boltzmann distribution with a radial flow profile can be used to describe the particle spectra [1]. However, the equilibrium distribution can only describe the very limited low p_T spectra and is sensitive to the choice of a specific p_T range. Tsallis statistics was introduced later in the literature to describe the particle production for an extended p_T range in high energy collisions [3–8]. One advantage of those Tsallis statistical analyses compared to the Boltzmann-Gibbs statistical one is that a new parameter is introduced in the model to describe the degree of nonequilibrium in the system, which is especially important for $p+p$ collisions [9] and peripheral A+A collisions [10]. It has been shown [11–14] that hard processes dominate the particle production for $p_T > 1.5$ GeV/c and the relativistic hard scattering for $p+p$ collisions leads to a transverse momentum distribution that resembles the Tsallis distribution. As pointed out in Ref. [13], the transverse momentum spectra of jets or the following hadron spectra from hard scattering satisfy a power law distribution, and the power index is closely related to the new degree of nonequilibrium parameter in Tsallis statistics. References [13,15–18] have depicted a synthesizing evolution from primary $p+p$ and peripheral A+A to central A+A collisions with the nonextensive statistical mechanical Tsallis distribution. A possible microcanonical generalization of the Tsallis distribution has been proposed

*li.yi@sdu.edu.cn

[14] which gives a good fit to data on fragmentation functions measured in e^+e^- collisions for $0.01 \leqslant x \leqslant 1$.

In relativistic heavy ion collisions, the system evolution is usually characterized by two stages of freeze-outs: the chemical freeze-out when further interactions (if any at all) do not alter the particle composition and the kinetic freeze-out when the momentum distribution of particles ceases to change. One could assume that the chemical and kinetic freeze-outs happen simultaneously at the hadronic and QGP phase boundary. At that moment, the system is at chemical and kinetic equilibrium with sudden freeze-out [19]. The short-lived resonances would decay and alter the kinetic spectra of the stable particles observed by experiments [20]. However, direct measurements of resonance suppression in the experiments at the Relativistic Heavy Ion Collider (RHIC) [11,21,22] and the Large Hadron Collider (LHC) [23] are not compatible with such a scenario. At the other extreme, one could assume that the chemical and kinetic freeze-outs occur at very different times. The resonances created at chemical freeze-out would decay quickly but the system continues to evolve with elastic collisions among hadrons (e.g., $\pi^+\pi^- \leftrightarrow \rho$) and is at local thermal equilibrium until kinetic freeze-out (BGBW) [24]. In this implementation, the stable hadrons are at kinetic equilibrium (with flow) and its kinematic distribution is indistinguishable from the resonance decay because they are at kinetic equilibrium (local detail balance) [25]. The nonequilibrium TBW is in-between these two extremes. TBW attempts to take nonequilibrium fluctuation and possible resonance decay (or the kinetic detail balance) in a consistent macroscopic approach. It is also possible to treat such a two-stage freeze-out in a microscopic model taking into account the resonance yields at the kinetic freeze-out and not from the resonance yields at the chemical freeze-out [26].

The collision energy dependence of radial flow velocity and kinetic freeze-out temperature in high energy heavy ion collisions has been an interesting subject in the community and been extensively studied for all available collision energies. In the energy range of the Heavy Ion Synchrotron to Super Proton Synchrotron, multiple studies agreed on an increasing trend for those two variables with an increase of the collision energy [27–29]. From RHIC to the LHC energy range, however, the interpretation of the experimental results is model dependent to date. For radial flow velocity, most studies found an increasing trend of flow velocity with increasing collision energy [27–33] but the quantitative value and whether there is sizable flow in $p+p$ and peripheral A+A collisions are model dependent. For kinetic freeze-out temperature, some studies claimed an increasing trend of kinetic freeze-out temperature with increasing collision energy [31,32] while others stated a decreasing trend [28,29,34–36], and some concluded little dependence on collision energy [27,30].

In this paper, to extract kinetic freeze-out temperature and radial flow velocity, we use the blast-wave model with Tsallis statistics [10,37,38] and compare to the Boltzmann-Gibbs statistics one [1,25,39] to simultaneously fit all the transverse momentum spectra of hadrons produced at mid-(pseudo)rapidity in $\sqrt{s_{\rm NN}} = 7.7$, 11.5, 14.5, 19.6, 27, 39, 62.4, and 200 GeV Au+Au collisions at RHIC [25,29,40–50] and in $\sqrt{s_{\rm NN}} = 2.76$ TeV [51–53] and 5.02 TeV [54] Pb+Pb collisions at the LHC. Such a systematic study on collision energy and centrality dependence of radial flow velocity, kinetic freeze-out temperature, and the degree of nonequilibrium from RHIC to the LHC energy range may shed light on the underlying physics in these collisions. Strange and multistrange particles, with smaller hadronic interaction cross-sections, are believed to decouple from the system earlier than hadrons with only light valence quarks [37,55–58]. The kinetic freeze-out behaviors of strange and multistrange particles are therefore also investigated separately.

This paper is organized as follows. In Sec. II, we describe the analysis method used in this paper. Results and discussions are given in Sec. III. The conclusion is summarized in the last section.

II. ANALYSIS METHOD

A. Blast-wave model

BGBW is a phenomenological model for hadron spectra based on flowing local thermal sources with global variables of temperature T and transverse flow profile β [1,2]. T is the temperature of the local thermal sources which particles radiate from. While the longitudinal expansion is assumed to be boost invariant, the transverse radial flow velocity of the thermal source is parametrized as $\beta(r) = \beta_S(\frac{r}{R})^n$ at radius $0 \leqslant r \leqslant R$ with surface velocity β_S and exponent n. The average radial flow velocity then can be written as $\langle\beta\rangle = \beta_S \times 2/(2+n)$ [59]. For an emitting source with Boltzmann-Gibbs distribution, the produced particle spectrum is therefore written in the form of

$$\left.\frac{d^2N}{2\pi p_T dp_T dy}\right|_{y=0} = A\int_0^R r dr m_T I_0\left(\frac{p_T \sinh(\rho)}{T}\right) \times K_1\left(\frac{m_T \cosh(\rho)}{T}\right), \quad (1)$$

where A is a normalization factor. $m_T = \sqrt{p_T^2 + m^2}$ is the transverse mass of a particle. I_0 and K_1 are the modified Bessel functions. $\rho = \tanh^{-1}\beta$. T is the kinetic freeze-out temperature. In order to compare with TBW results, we take $n = 1$ for the BGBW model in this paper. With common freeze-out temperature T and average radial flow velocity $\langle\beta\rangle$, the shape of the spectrum for each particle species is determined by its mass in BGBW.

B. Tsallis blast-wave model

TBW [10,37,38,59] is modified from the standard BGBW model when a Tsallis statistics replaces the conventional Boltzmann-Gibbs statistics for the particle emission distribution. The invariant differential particle yield in TBW is then written in the form of

$$\left.\frac{d^2N}{2\pi m_T dm_T dy}\right|_{y=0} = A\int_{-y_b}^{+y_b} e^{\sqrt{y_b^2 - y_s^2}} m_T \cosh(y_s) dy_s \times \int_0^R r dr \int_{-\pi}^{\pi}\left[1 + \frac{q-1}{T}E_T\right]^{-1/(q-1)} d\phi, \quad (2)$$

TABLE I. Spectra data references.

System	$\sqrt{s_{\rm NN}}$ (GeV)	Particle	Collaboration	Reference
Au+Au	7.7, 11.5, 19.6, 27	$\pi^{\pm}$, $K^{\pm}$, p, $\bar{p}$	STAR	[29]
		K^0_s, Λ, $\bar{\Lambda}$, Ξ^+, Ξ^-	STAR	[44]
Au+Au	14.5	$\pi^{\pm}$, $K^{\pm}$, p, $\bar{p}$	STAR	[40]
Au+Au	39	$\pi^{\pm}$, $K^{\pm}$, p, $\bar{p}$	STAR	[29]
		K^0_s, Λ, $\bar{\Lambda}$, Ξ^+, Ξ^-	STAR	[44]
		π^0	PHENIX	[47]
Au+Au	62.4	$\pi^{\pm}$, $K^{\pm}$, p, $\bar{p}$	STAR	[25]
		$\pi^{\pm}$, p, $\bar{p}$	STAR	[41]
		K^0_s, Λ, $\bar{\Lambda}$, Ξ^+, Ξ^-, Ω^+, Ω^-	STAR	[45]
		ϕ	STAR	[46]
		π^0	PHENIX	[47]
Au+Au	200	$\pi^{\pm}$, p, $\bar{p}$	STAR	[43]
		$K^{\pm}$	STAR	[42]
		$K^{\pm}$	PHENIX	[48]
		Λ, $\bar{\Lambda}$, Ξ^+, Ξ^-, Ω	STAR	[49]
		ϕ	STAR	[50]
Pb+Pb	2760	$\pi^{\pm}$, $K^{\pm}$, p, $\bar{p}$	ALICE	[51]
		K^0_s, Λ	ALICE	[52]
		Ξ^+, Ξ^-, Ω^+, Ω^-	ALICE	[53]
Pb+Pb	5020	$\pi^{\pm}$, $K^{\pm}$, p, $\bar{p}$	ALICE	[54]

where

$$E_T = m_T \cosh(y_s)\cosh(\rho) - p_T \sinh(\rho)\cos(\phi). \quad (3)$$

y_s is the source rapidity. y_b is the beam rapidity. ϕ is the particle emission angle in the rest frame of the thermal source. q is the parameter characterizing the degree of nonequilibrium of the produced system, which is the new parameter introduced in TBW compared to the BGBW model. Although the applicability of such a model to high energy nuclear collisions is still under investigation, possible physics implications are available in the literature. The initial energy density in heavy ion collision has multiple hot spots caused by color-glass condensate formation in a nucleon or individual nucleon-nucleon collisions. Those hot spots are dissipated into the system, producing more particles, generating collective flow, and resulting in a temperature fluctuation at the initial state [4,60]. The initial state fluctuation is not guaranteed to be completely washed out by the medium, in QGP or hadron gas phases. The survived fluctuation will leave imprints in spectra at low and intermediate p_T range. Such features in spectra will lead to q values larger than 1 in the TBW model [59]. When $q = 1$, Eq. (2) recovers its familiar Boltzmann-Gibbs form.

In this paper, we also use a Tsallis blast-wave model with four fit parameters with different q for mesons and baryons separately, referred to as TBW4. TBW4 was first proposed in Ref. [10] for a better description of meson and baryon spectra at $p + p$ collisions while the TBW fits with one single q for all particles gave a very poor χ^2/nDoF. TBW without further description in this paper refers to the default one with three fit parameters, that is, the one using the same q for both mesons and baryons.

III. RESULTS AND DISCUSSIONS

A. Transverse momentum spectra

This section compares three blast-wave model fits of the transverse momentum spectra. Table I lists the particle spectra data used in this paper. Those particle spectra form two species groups for the fit procedure: one with all available hadrons, and another with charged pion, kaon, proton, and antiproton only. The first group aims to identify the common freeze-out properties for all particles. The latter is chosen to be consistent with previous publications [29] for an apple-to-apple comparison. The reported experimental systematic and statistical uncertainties are combined as a quadratic sum for the fitting procedures. For all fit procedures, the average flow velocity $\langle\beta\rangle$ is limited to the range of $0 \leqslant \langle\beta\rangle \leqslant 2/3$ [25] for a better convergence in fitting and to avoid nonphysical results (negative value or faster than the speed of light) [10]. Furthermore, spectra fit range is limited to $p_T \leqslant 3$ GeV/c in order to have a comparable p_T range for all energies and to focus on the bulk properties. For the sake of concision, this section only shows the fits to spectra for all particles in most central and most peripheral centrality classes at four collision energies as examples in Figs. 1 to 4. The fit results for all centrality classes at all studied collision energies can be found in Table III to XIII. Figure 1 (Fig. 2) shows blast-wave fits to identified particle transverse momentum spectra in most central (most peripheral) collisions, with corresponding deviations of those fits to experimental data divided by data uncertainties shown in Fig. 3 (Fig. 4). The fit results of kinetic freeze-out parameters for both species groups at various centrality classes and collision energies are discussed in the next section. Those extracted fit

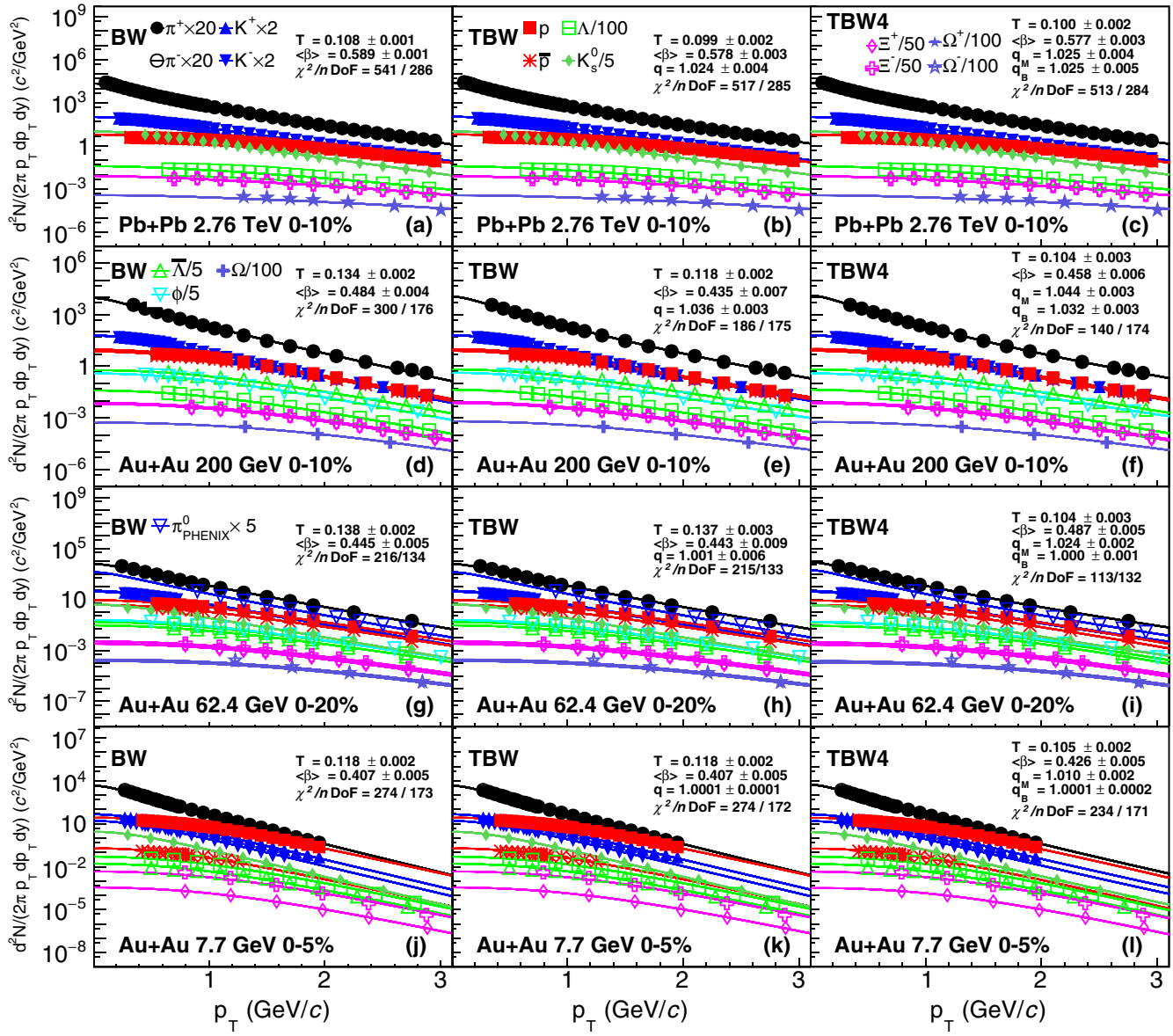

FIG. 1. Blast-wave model fits to hadron spectra in most central Pb+Pb and Au+Au collisions at $\sqrt{s_{\mathrm{NN}}} = 2.76$ TeV, 200 GeV, 62.4 GeV, and 7.7 GeV from top to bottom panels. The different symbols represent experimental data of different particle species. Uncertainties on experimental data represent quadratic sums of statistical and systematic uncertainties. The solid curves represent fit results for BGBW (left column), TBW (middle column), and TBW4 (right column).

parameters and $\chi^2/n\mathrm{DoF}$ of TBW models are also summarized in Tables III to XIII.

BGBW and TBW models are compared in the left and middle panels of Figs. 1 to 4. From top to bottom panels of each figure, the spectra (Figs. 1 and 2) or difference between model and experiment data divided by the error of data (Figs. 3 and 4) in Pb+Pb or Au+Au collisions at $\sqrt{s_{\mathrm{NN}}} = 2.76$ TeV, 200 GeV, 62.4 GeV, and 7.7 GeV are presented. At LHC and top RHIC energies, the deviation of the BGBW model from experimental data is larger in peripheral than in central collisions. As beam energy decreases, the deviation of BGBW model fit from data decreases. We note that there are fewer experimental data at $p_T > 2$ GeV/c for energies below 39 GeV. Overall, TBW has better fits and has smaller $\chi^2/n\mathrm{DoF}$ than BGBW. TBW agrees with most data points within three-σ standard deviation from experimental data. TBW yields a smaller q toward lower beam energy, which indicates that the system is closer to equilibrium state toward lower energy. For all LHC and RHIC energies, TBW fits in peripheral collisions have larger q values than those in central collisions at the same collision energy. In short, the TBW model performs much better than BGBW and the nonequilibrium seems to be necessary for peripheral collisions at high energies. As the BGBW model assumes thermal equilibrium and the TBW model uses nonequilibrium statistics, the above observations suggest that the collision system deviates more from thermal equilibrium at higher energy, especially in peripheral collisions.

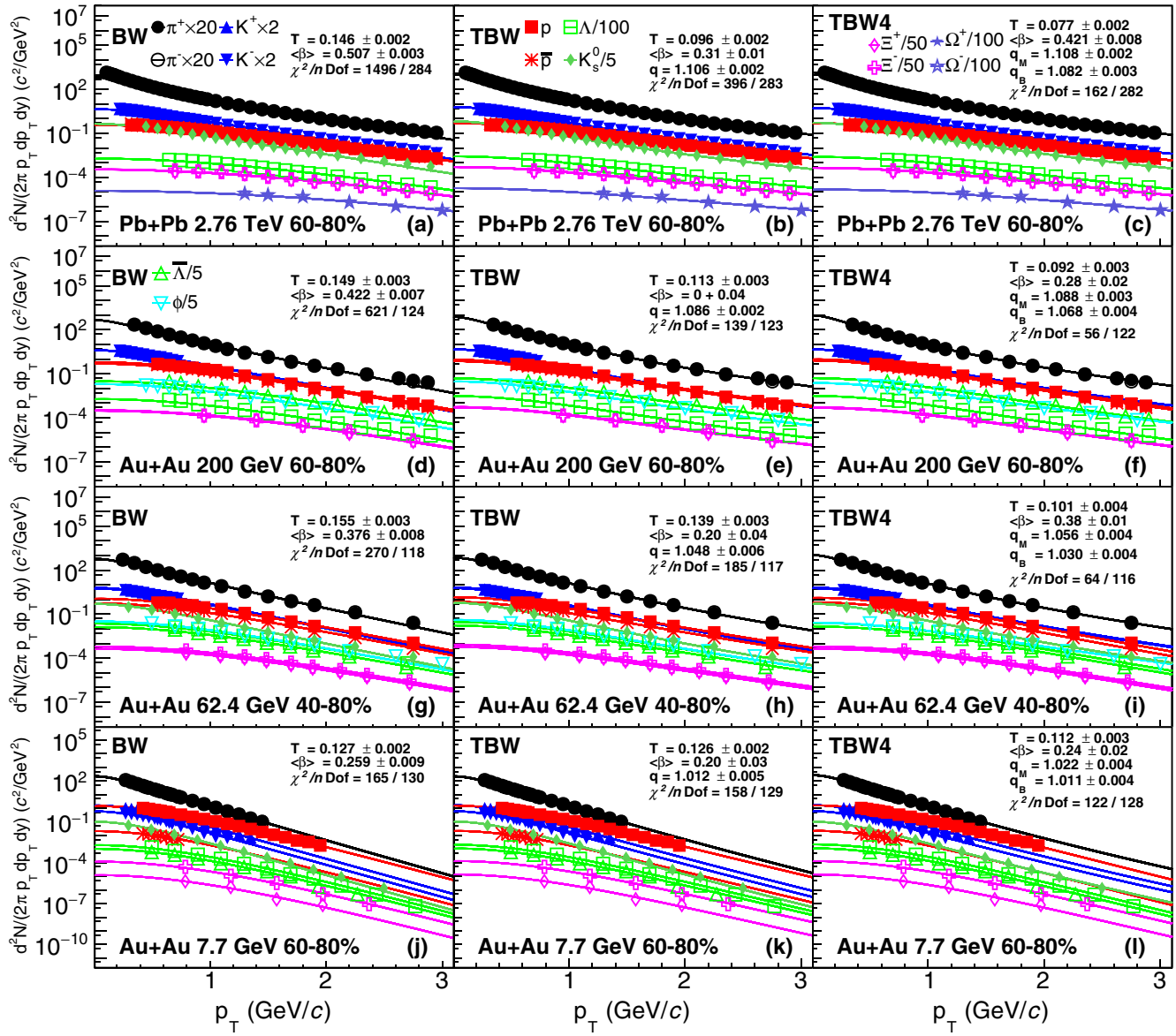

FIG. 2. Same as Fig. 1, but for most peripheral collisions.

The comparison of TBW (with a single q) and TBW4 (with separate q for meson and baryon) is shown in the middle and right panels of Figs. 1 to 4. TBW4 has even smaller χ^2/nDoF than TBW for all LHC and RHIC energies, while the improvement is larger in peripheral than central collisions. For TBW4, the nonequilibrium parameter q of baryons is found to be smaller than that of mesons, as baryons have steeper spectra than mesons. Baryons used in the fitting include mostly strange (Λ) and multistrange (Ξ and Ω) particle species and strangeness has smaller q value and higher freeze-out temperature. More details on different freeze-out will be discussed later in Sec. III B.

B. Kinetic freeze-out parameters

The extracted results for temperature T and average radial flow velocity $\langle\beta\rangle$ from BGBW, TBW, and TBW4 are compared in Figs. 5 and 6. The beam energy, centrality, and particle species dependences of T, $\langle\beta\rangle$, and q from the TBW model are investigated in Figs. 7 and 8.

The dependence of T on $\langle\beta\rangle$ of BGBW, TBW, and TBW4 is shown in Fig. 5 for charged pions, kaons, and protons, and in Fig. 6 for all available hadrons including strange and multistrange particles. Symbols with same color represent A+A collisions at same beam energy for different centrality classes. In general, fit parameters in Fig. 6 for all particles have smaller fit uncertainties than those in Fig. 5 for charged pions, kaons, and protons only, as more particles are used to study their common freeze-out properties. Other than that, these two species groups give similar results for T dependence on $\langle\beta\rangle$. BGBW results shown on the left panel display an anticorrelation between T and $\langle\beta\rangle$. At the same collision energy, T decreases and $\langle\beta\rangle$ increases as the system moves from peripheral to central collisions. As collision energy increases,

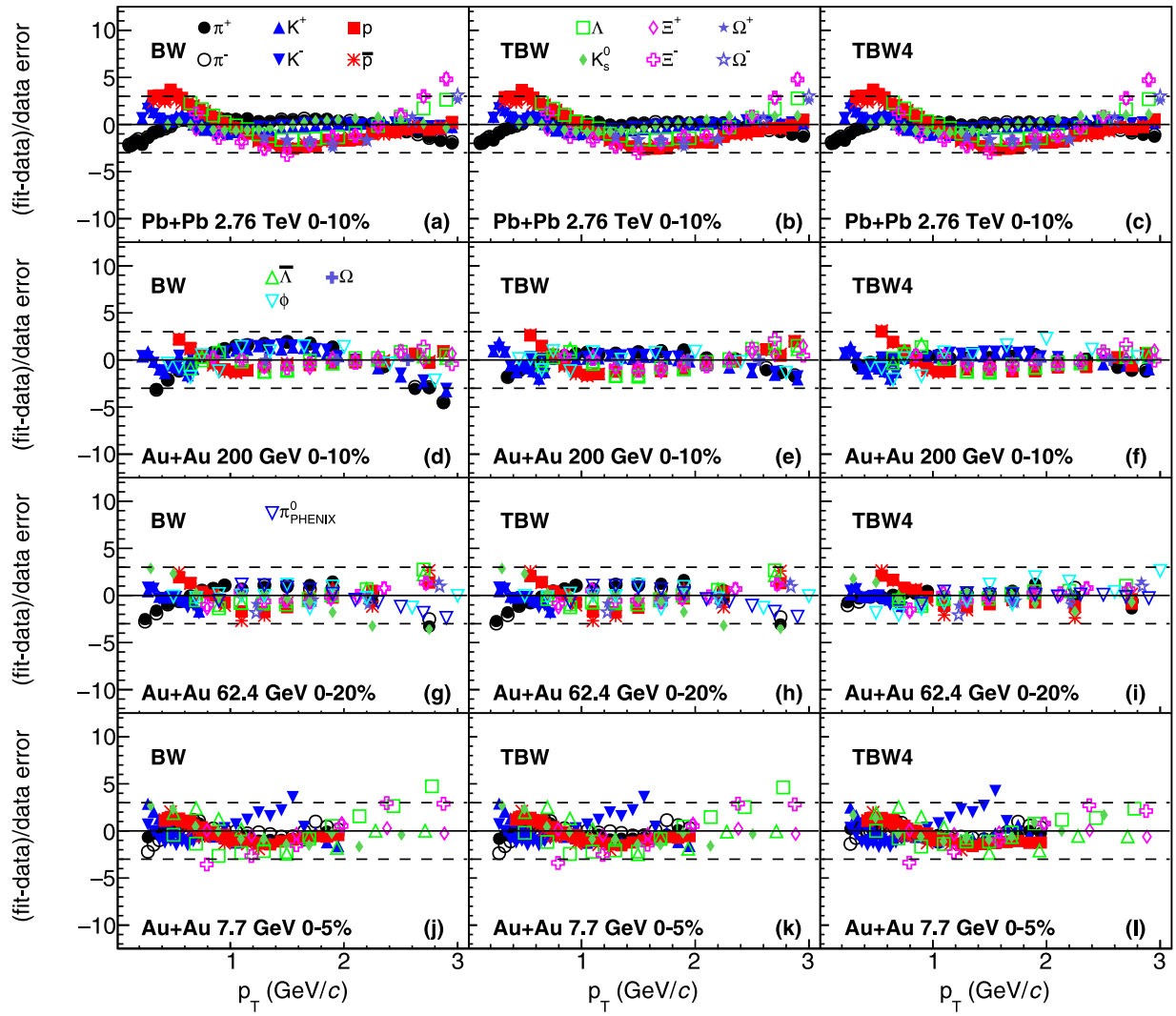

FIG. 3. The deviations of BGBW (left column), TBW (middle column), and TBW4 model fits to hadron spectra divided by data uncertainties in most central Pb+Pb and Au+Au collisions at $\sqrt{s_{\rm NN}} = 2.76$ TeV, 200 GeV, 62.4 GeV, and 7.7 GeV from top to bottom panels. The different symbols are used to distinguish particle species. The dashed lines represent where the difference between model and experiment data is three times the error of data.

the anticorrelation curve moves toward high $\langle\beta\rangle$. Such anticorrelation behavior was also reported in Ref. [29]. TBW results in the middle panel, however, are different from BGBW ones. T from TBW has much weaker dependence on centrality than the BGBW one. For example, at the LHC energies, the increase of T from most central to most peripheral collisions is around 40% in BGBW. In contrast, the variation of T is only about 5% in TBW. Similar behavior of weak centrality dependence for temperature was also reported in Ref. [20], when further resonance decay after sudden equilibrium freeze-out is considered in BGBW. The resonance decay is one of the microscopic nonequilibrium sources in the macroscopic TBW approach. The common observation from these two studies supports the expectation that the strong centrality dependence of freeze-out temperature in the BGBW model is rooted in its incapability to describe the nonequilibrium system. The parameter $\langle\beta\rangle$ in most central collisions from TBW is between 0.4 and 0.5 for RHIC energies and around 0.6 at the LHC, similar with those in BGBW. In peripheral collisions $\langle\beta\rangle$ is lower in TBW than that in BGBW, while it even reaches zero value for the most peripheral collisions at RHIC energies. It seems that from the TBW model's viewpoint hadron scatterings (or QGP droplets if any) are not sufficient to produce a large collective radial flow or to maintain a thermal equilibrium in peripheral collisions at RHIC. The BGBW model, while lacking a knob for nonequilibrium degree, has to boost its radial flow parameter in a struggle to fit the high yields of the spectra at intermediate p_T in the peripheral collisions. In Figs. 5 and 6, T and $\langle\beta\rangle$ from TBW4 on the right panels are similar to those from TBW with one single q in the middle panels and different from those from BGBW on the left panels. There is a weaker centrality dependence for T and lower $\langle\beta\rangle$ values at peripheral collisions for both TBW models than BGBW. We observed that at the LHC energies T and $\langle\beta\rangle$ from TBW4 tend to have a positive correlation rather than anticorrelation as in BGBW fits or a lack of correlation as in default TBW. The fit

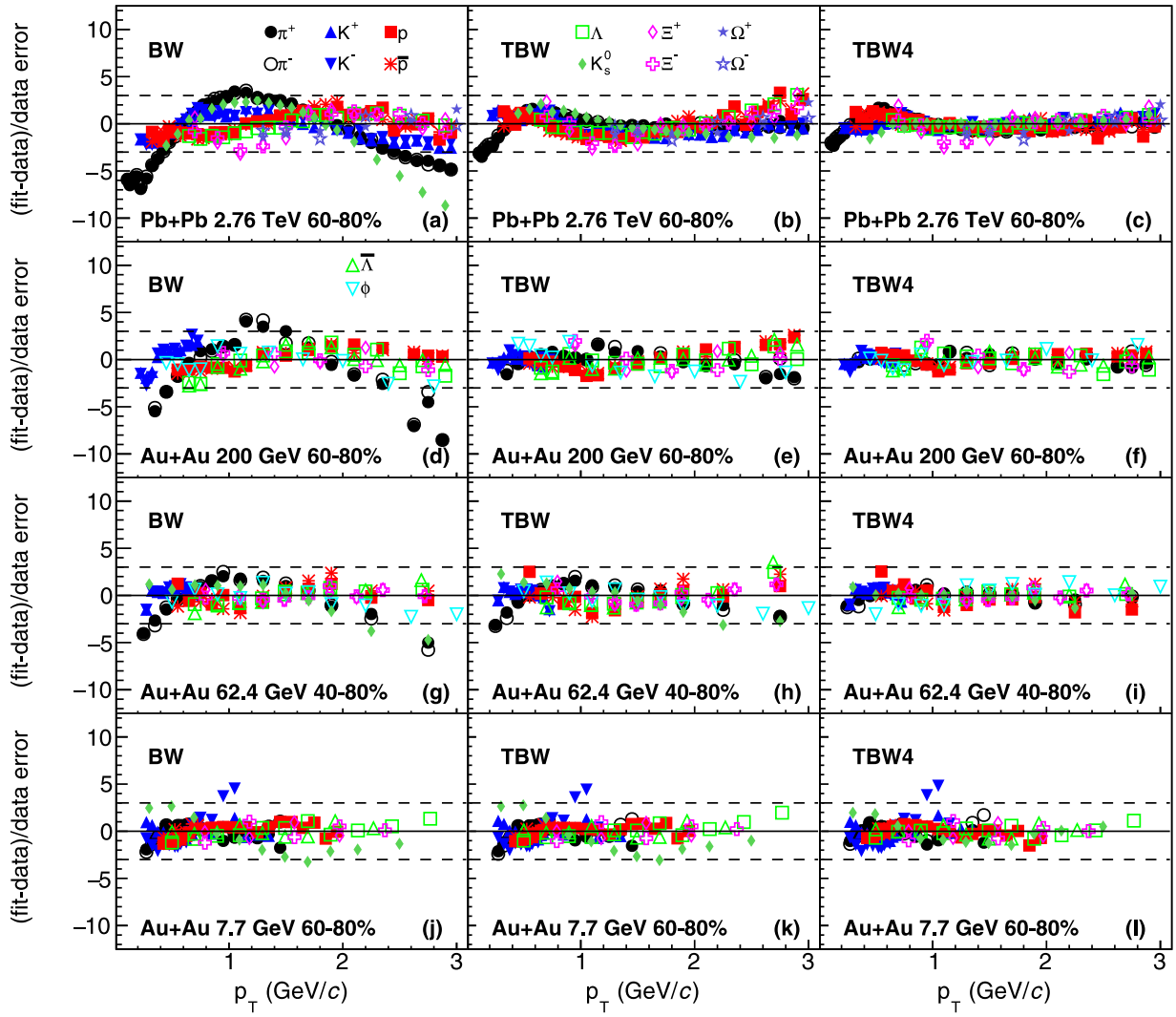

FIG. 4. Same as Fig. 3, but for most peripheral collisions.

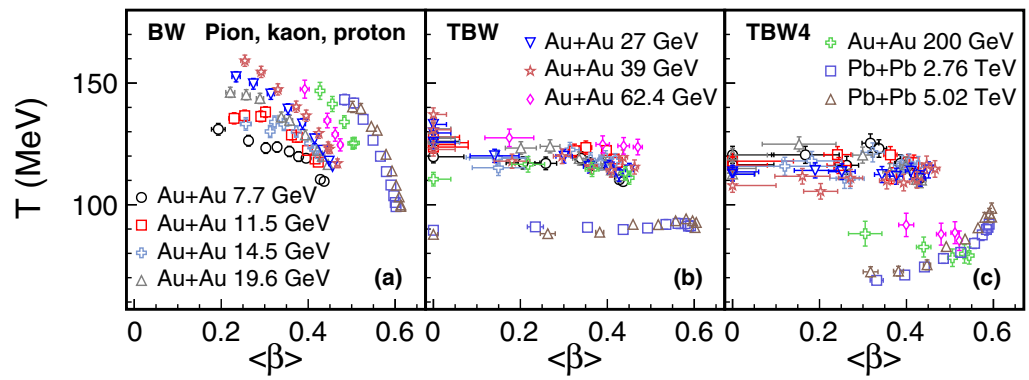

FIG. 5. Variation of T with $\langle\beta\rangle$ for different energies and centralities from BGBW (left panel), TBW (middle panel), and TBW4 (right panel) fits to p_T spectra of only positive and negative pions, kaons, and protons. Symbols with the same style represent different centrality classes at the same colliding energy. For a given energy, from left to right, the centrality moves from peripheral to central collision.

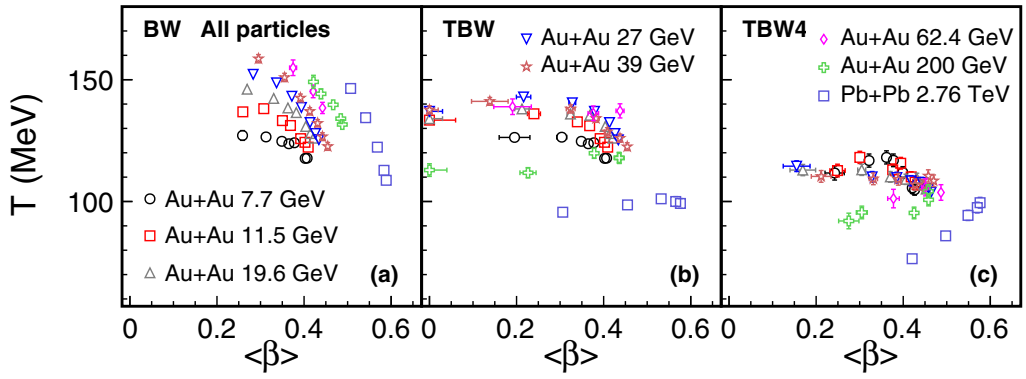

FIG. 6. Same as Fig. 5, but for all hadrons including strange and multistrange particles.

parameter values are slightly different for the two TBW models as discussed below. In Fig. 5, for charged pions, kaons, and protons, T from TBW4 is lower than the one in default TBW at $\sqrt{s_{\rm NN}}$ above 62.4 GeV. For lower beam energies, within the uncertainties, T values from these two models appear to be consistent. For the cases including all hadrons and shown in Fig. 6, the results are in general with smaller uncertainties of all the fit parameters, and T from the TBW4 are lower than

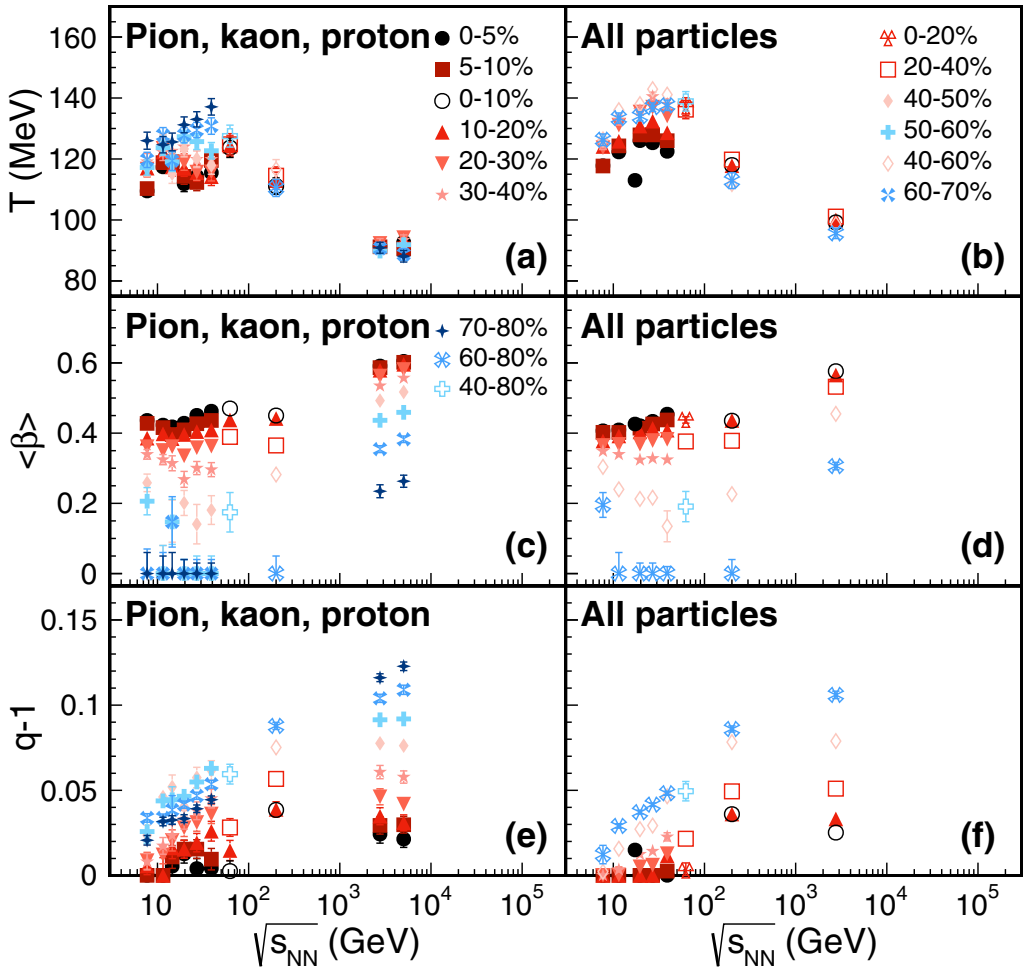

FIG. 7. Collision energy dependence of the extracted kinetic freeze-out parameters for heavy ion collisions of different centralities in TBW fits of p_T spectra for only positive and negative pions, kaons, and protons (left column), and all particles (right column). The kinetic freeze-out temperature T, average transverse radial flow velocity $\langle\beta\rangle$, and nonequilibrium parameter $q-1$ are shown in the top, middle, and bottom panels, respectively. The results for all particles in most central Pb+Pb collisions at $\sqrt{s_{\rm NN}} = 17.3$ GeV are from Ref. [37].

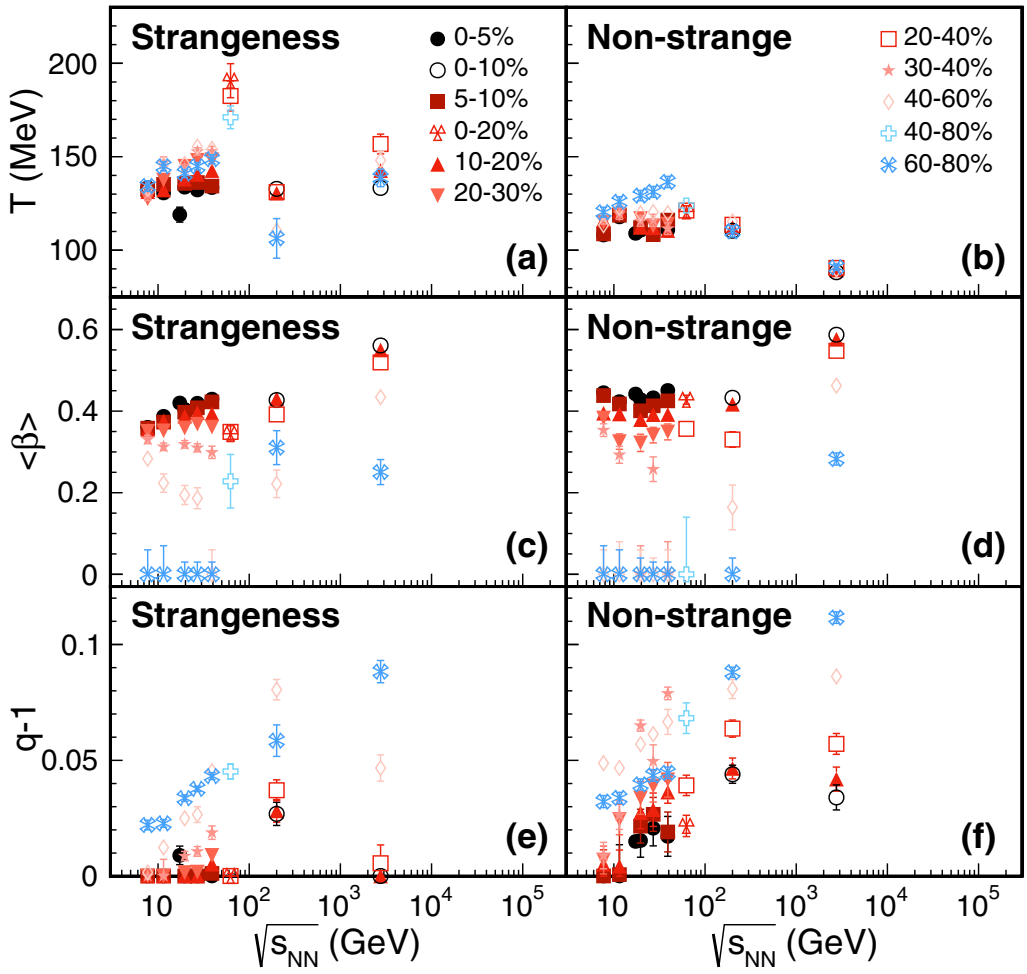

FIG. 8. Same as Fig. 7, but for strangeness only (left column), and nonstrange particles (right column). The results in most central Pb+Pb collisions at $\sqrt{s_{\rm NN}} = 17.3$ GeV are from Ref. [37].

the default TBW for all the energies. The main observation from the comparison of BGBW and two TBW models is that T in TBW models has weaker centrality dependence and $\langle\beta\rangle$ at peripheral collisions is lower than those in BGBW.

Figure 7 shows the energy and centrality dependence of kinetic freeze-out parameters T, $\langle\beta\rangle$, and $(q-1)$ from the TBW model for charged pions, kaons, and protons in the left column and for all particles in the right column. The kinetic freeze-out temperature T in panel (a) and (b) of Fig. 7 shows weak collision energy dependence at $\sqrt{s_{\rm NN}}$ of 7.7–39 GeV, while it drops from $\sqrt{s_{\rm NN}} = 62.4$ GeV to 5.02 TeV in panel (a) and 2.76 TeV in panel (b). At 7.7–39 GeV, at any given collision energy, T only decreases marginally from peripheral to central collisions. At 62.4 GeV to 5.02 TeV, the centrality dependence of T is even smaller. In contrast, as discussed in the previous section, in BGBW, T decreases notably from peripheral to central collisions. In most of the peripheral collisions, BGBW deviates significantly from data with larger χ^2/nDoF. Meanwhile, the nonequilibrium parameter q in TBW for peripheral collisions also increases with increasing collision energy as shown in the bottom two panels of Fig. 7. The strong centrality dependence of T in BGBW may be synthetic to the model's incapacity to incorporate the large nonequilibrium effect of the system in the peripheral collisions. The average transverse radial flow velocity $\langle\beta\rangle$ shown in panel (c) and (d) of Fig. 7, for most central collisions, is between 0.4 and 0.5 at RHIC energies, and around 0.6 at the LHC energies. $\langle\beta\rangle$ decreases from central to peripheral collisions. In most peripheral collisions, $\langle\beta\rangle$ drops to zero at RHIC energies and is less than 0.3 at the LHC energies. For the most peripheral collisions at RHIC, the system in general fails to generate a rapid radial expansion. The nonequilibrium parameter $(q-1)$ in panel (e) and (f) of Figure 7 is small in central Au+Au collisions, suggesting that the produced particles are approaching thermal equilibrium. In peripheral collisions, $(q-1)$ increases from less than 0.04 at 7.7 GeV to more than 0.1 at 5.02 TeV, indicating an increasing deviation from Boltzmann statistics as collision energy increases. The centrality dependence of the $(q-1)$ parameter suggests an evolution from an almost thermalized system in the central collisions towards a highly off-equilibrium system in the peripheral collisions. Such large $(q-1)$ is also found in the study of $p+p$ collision [9]. This may be because the energy density fluctuations at initial

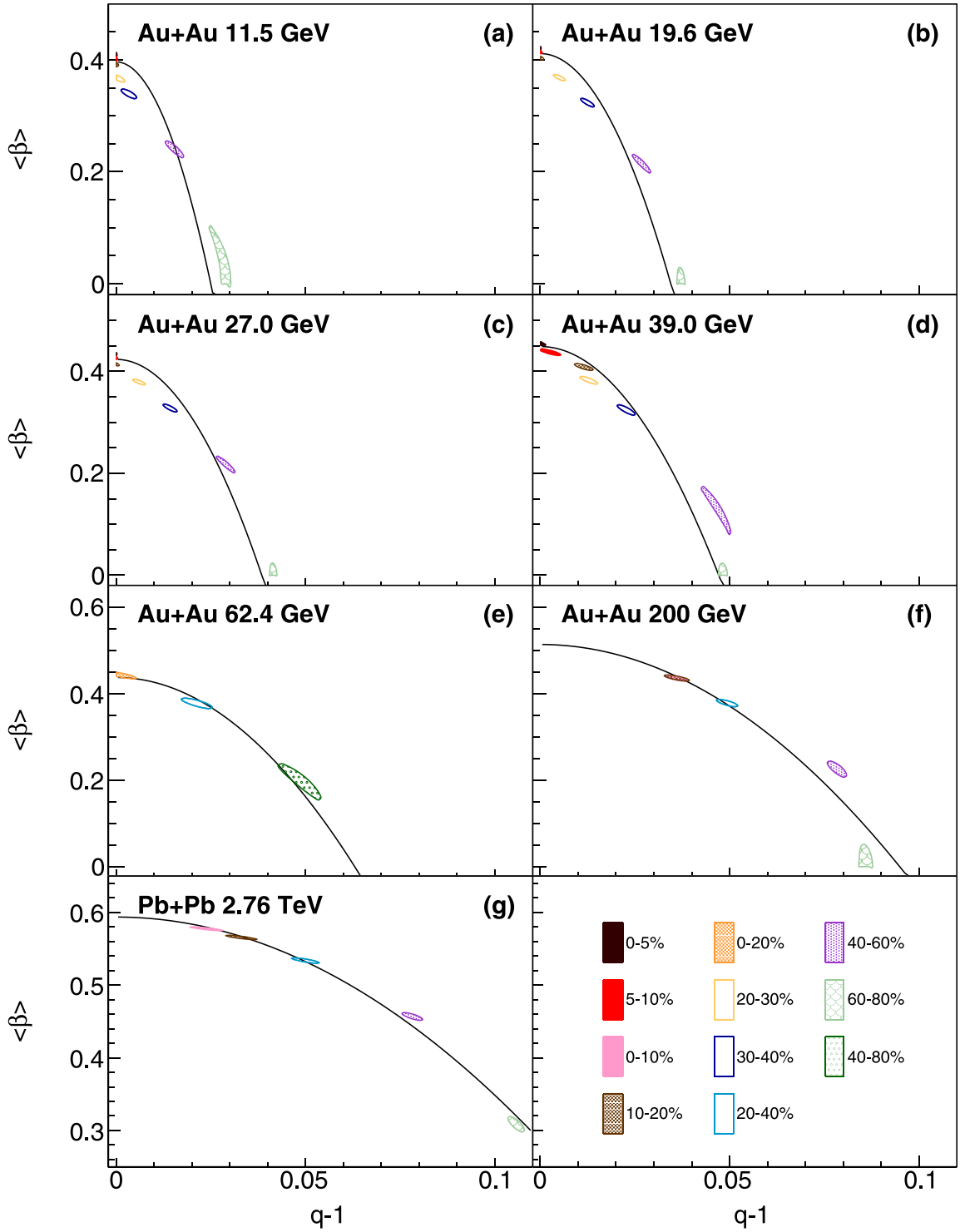

FIG. 9. Extracted average radial flow velocity $\langle\beta\rangle$ as a function of nonequilibrium degree $(q-1)$ obtained in TBW fits of p_T spectra of all particles. Each block is a one-σ contour from the error matrix of the TBW fit for a given centrality of Au+Au (Pb+Pb) collisions. The curves represent quadratics fits in the form of $\langle\beta\rangle = \langle\beta\rangle_0 - a(q-1)^2$.

state due to color-glass condensate formation or individual hard scattering (minijets) inside a nucleus-nucleus collision increase as collision energy increases. Such fluctuations are not completely washed out by subsequent QGP evolution or hadronic interactions and leave footprints in final state particle spectra at the p_T range in our paper [10].

In general, the group of charged pion, kaon, and proton and the group of all particles as shown in Fig. 7 produce similar

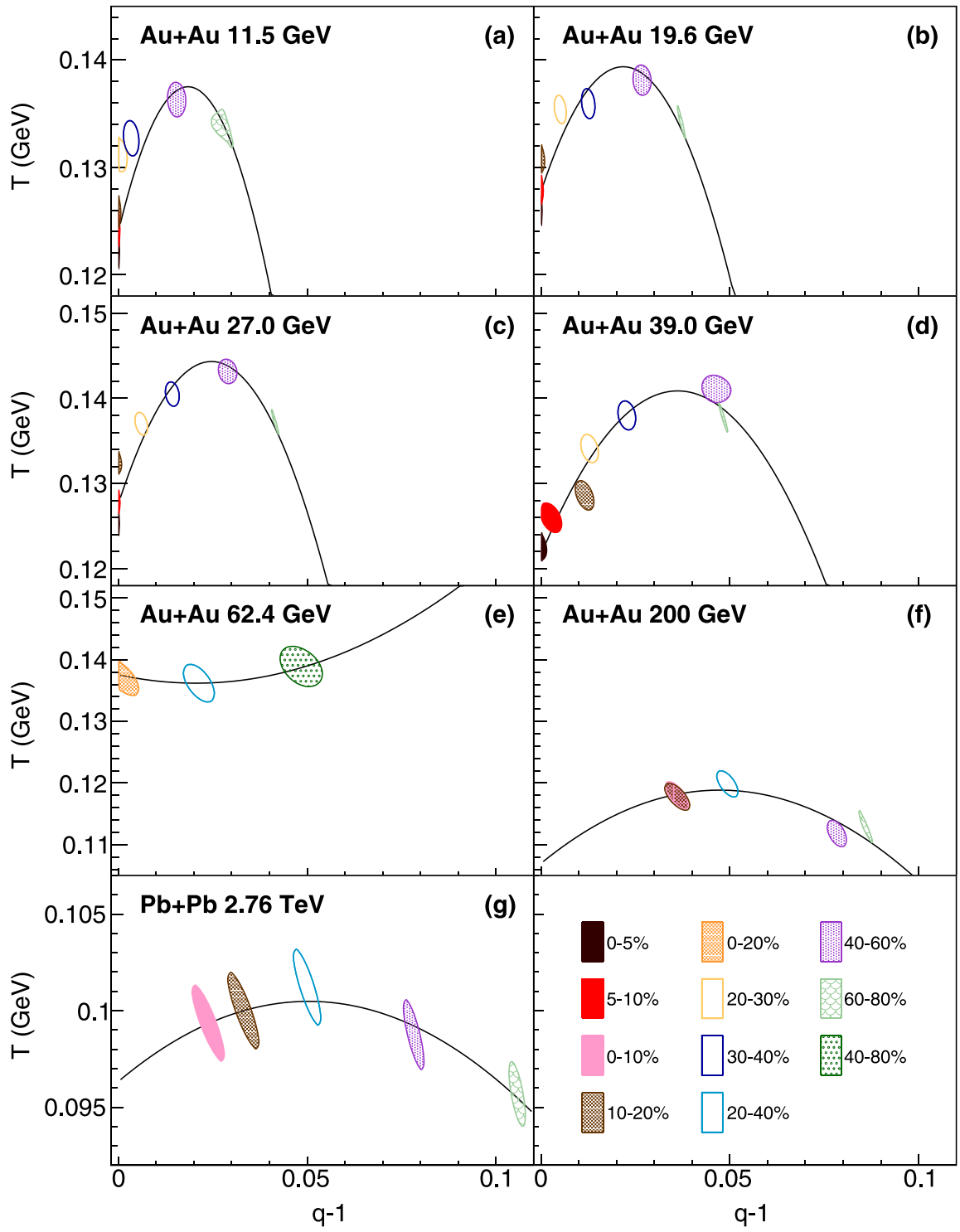

FIG. 10. Extracted kinetic freeze-out temperature T as a function of nonequilibrium degree $(q-1)$ obtained in TBW fits of p_T spectra of all particles. Each block is a one-σ contour from the error matrix of the TBW fit for a given centrality of Au+Au (Pb+Pb) collisions. The curves represent quadratics fits in the form of $T = T_0 + b(q-1) - d\xi(q-1)^2$.

kinetic freeze-out parameters in TBW fits. Small difference can be identified with slightly higher T and lower q for the group with all particles than that with only the $\pi/K/p$. Such difference may come from the influence of particle species as the group of all particles contains more strange particles. The direct comparison of nonstrange and strangeness in Fig. 8 confirms that the strange hadrons have higher temperature (T) and a smaller nonequilibrium degree (q) than those of

TABLE II. The fitting parameters of $\langle\beta\rangle = \langle\beta\rangle_0 - a(q-1)^2$ in Fig. 9 and $T = T_0 + b(q-1) - d\xi(q-1)^2$ in Fig. 10.

System	$\sqrt{s_{\rm NN}}$ (GeV)	$\langle\beta\rangle_0$	a	T_0 (GeV)	b	$d\xi$
Au+Au	11.5	0.397 ± 0.002	635 ± 88	0.1240 ± 0.0009	1.5 ± 0.2	40 ± 9
Au+Au	19.6	0.411 ± 0.002	347 ± 27	0.1278 ± 0.0008	1.1 ± 0.2	25 ± 5
Au+Au	27	0.423 ± 0.002	286 ± 20	0.1277 ± 0.0008	1.4 ± 0.2	27 ± 4
Au+Au	39	0.448 ± 0.002	202 ± 14	0.122 ± 0.002	1.1 ± 0.2	15 ± 4
Au+Au	62.4	0.44 ± 0.01	110 ± 28	0.138 ± 0.004	$-(0.1 \pm 0.4)$	$-(3 \pm 7)$
Au+Au	200	0.51 ± 0.02	57 ± 6	0.11 ± 0.02	0.5 ± 0.7	5 ± 5
Pb+Pb	2760	0.594 ± 0.005	25 ± 1	0.096 ± 0.005	0.2 ± 0.2	2 ± 1

nonstrange hadrons, while their radial flow values ($\langle\beta\rangle$) are similar. A higher temperature indicates an earlier decoupling of strange hadrons from the system. The smaller q in the strangeness group than the nonstrangeness group and a similar $\langle\beta\rangle$ between those two groups suggest that the system is closer to an equilibrium state when the strangeness hadrons decouple from the system and further hadronic interactions do not increase the system's radial flow velocity. A possible conclusion is that the hadronic phase does not increase radial flow of light hadrons significantly at RHIC and LHC energies, and instead drives the system toward nonequilibrium: the system in central collisions has approached thermal equilibrium at the partonic phase, and the later hadronic scattering drives the system off equilibrium and does not increase the radial flow of copiously produced light hadrons [37]. Another interesting observation is that in Fig. 8(b) for nonstrange particles the kinetic freeze-out temperature of the central collisions decreases from RHIC to LHC energies in the TBW model, while in Fig. 8(a) strangeness does not show this behavior. A possible explanation is that the system at the LHC has higher flow velocity and larger volume than that at RHIC and maybe needs more time for all particles to kinetic freeze-out ("cool") in the expansion during the hadronic phase.

It has been argued within the framework of nonequilibrium statistics that the dependence of temperature and flow velocity on the nonequilibrium factor $(q-1)$ is related to the shear and bulk ξ viscosity in linear or quadratic proportion [4,12]. This hypothesis is examined by quadratic fits of $\langle\beta\rangle = \langle\beta\rangle_0 - a(q-1)^2$ and $T = T_0 + b(q-1) - d\xi(q-1)^2$ (where ξ is the bulk viscosity) to the inclusive hadron group as shown in Figs. 9 and 10 with fit parameters and χ^2/nDoF listed in Table II. Data at 7.7 GeV are close to equilibrium and do not provide a significant variation of the parameters, and are not included in this examination. From 11.5 to 2.76 TeV collision energy, there displays a clear evolution of $\langle\beta\rangle$ vs $(q-1)$ and T vs $(q-1)$ relationships on collision energy. A summary of parameters $\langle\beta\rangle_0$, a, T_0, b, and $d\xi$ dependence on collision energy is depicted in Figs. 11 and 12. As energy increases, $\langle\beta\rangle_0$ increases and the coefficient of the squared term a decreases. A similar feature is observed for the T vs $(q-1)$. With only three available centrality classes, the fitting procedure at 62.4 GeV is found to be not constrained. The relationship of T vs $(q-1)$ was previously inspected in Ref. [10] for 200 GeV where only a squared term (with a constant) is used. Our paper shows that both linear and quadratic terms are needed to describe the T vs $(q-1)$ relationship for lower collision energies. The linear term parameter b and quadratic term related to viscosity parameter $d\xi$ show a trend of decrease with collision energy. It is interesting to note that it has been argued that the bulk viscosity increases dramatically toward the phase transition [61,62], coinciding with the feature we observed of $d\xi$ shown in Fig. 12.

In a short summary, BGBW and TBW have been used to explore the beam energy dependence of kinetic freeze-out properties of the system created in relativistic heavy ion collisions. The BGBW model is designed to describe the system in local thermal equilibrium. However, as collision energy increases, the produced system in peripheral collisions deviates far from equilibrium state, and cannot be described well with a BGBW fit. An additional parameter q is introduced in the

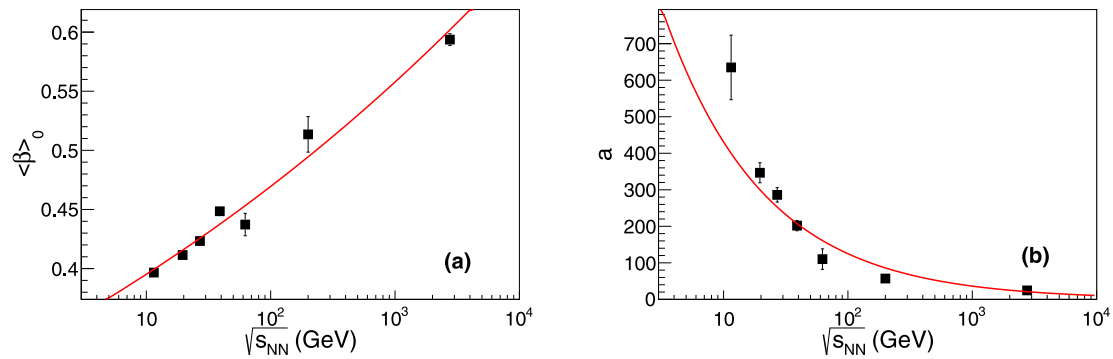

FIG. 11. Collision energy dependence of parameters $\langle\beta\rangle_0$ and a in $\langle\beta\rangle = \langle\beta\rangle_0 - a(q-1)^2$. Curves are to guide the eye.

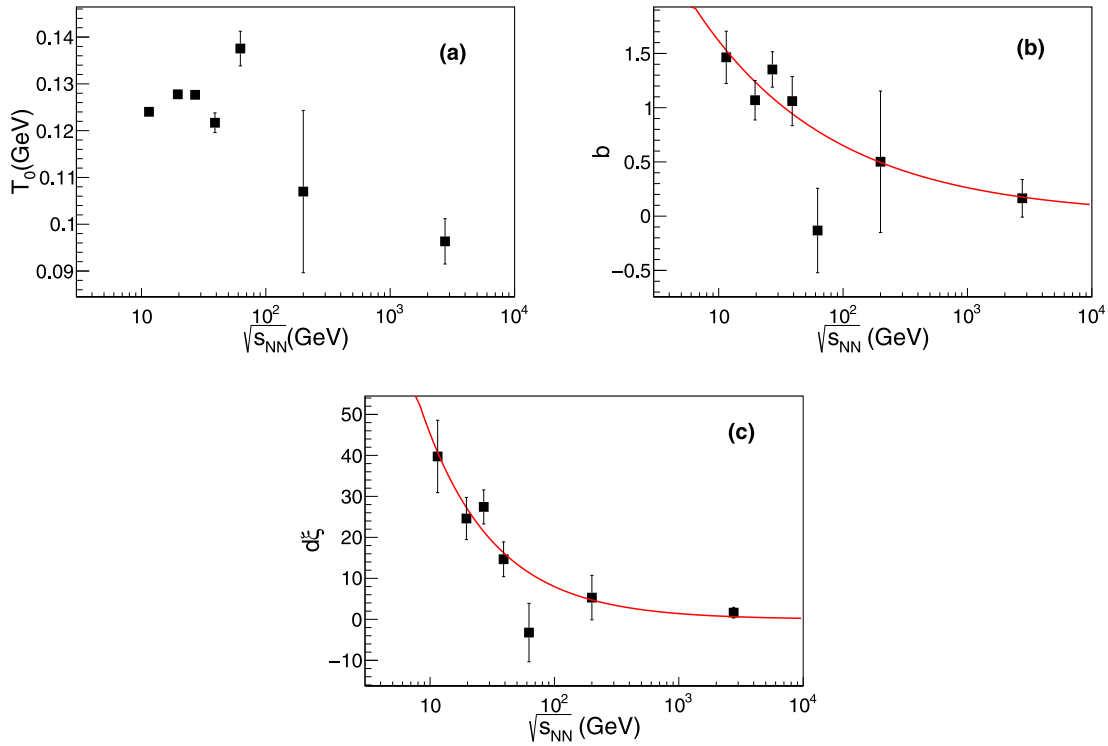

FIG. 12. Collision energy dependence of parameters T_0, b, and $d\xi$ in $T = T_0 + b(q-1) - d\xi(q-1)^2$. Curves are to guide the eye.

TBW model to characterize the degree of nonequilibrium. The divergence between BGBW and TBW escalates with an increasing q value as collision energy increases, especially in peripheral collisions. For 7.7–39 GeV collision energies, the increase of temperature in the TBW model from central to peripheral collisions is much less than that in BGBW. For 62.4 GeV to 5.02 TeV, the temperature in the TBW model stays almost constant from central to peripheral collisions. Meanwhile, the radial flow value in central collisions is around 0.4–0.5c at RHIC energies, and becomes larger at the LHC energies.

IV. CONCLUSION

In this paper, we have used the blast-wave model with Boltzmann-Gibbs statistics and with Tsallis statistics to fit the transverse momentum spectra of hadrons produced at mid-(pseudo)rapidity in Au+Au collisions at $\sqrt{s_{NN}} = 7.7$, 11.5, 14.5, 19.6, 27, 39, 62.4, and 200 GeV at RHIC and in Pb+Pb collisions at $\sqrt{s_{NN}} = 2.76$ TeV and 5.02 TeV at LHC to extract kinetic freeze-out temperature and transverse flow velocity and to study their collision centrality and energy dependence. The hadrons containing strangeness at those collision energies were also examined to study their impact on the freeze-out properties. For centrality dependence, the results show that the average transverse radial flow velocity decreases and the degree of nonequilibrium q increases from central to peripheral collisions in the TBW model. The kinetic freeze-out temperature shows weak dependence on centrality in the TBW model, while in the BGBW model there is a clear increase from central to peripheral in A+A collisions. This finding suggests that a change in nonequilibrium degree of the system in TBW is reflected as a change in freeze-out temperature in the language of transitional BGBW. One should take caution when interpreting temperature behavior in BGBW for beam energy scan results. For energy dependence in TBW fits, the average transverse radial flow velocity and the degree of nonequilibrium q both increase with the increase of the collision energy, which suggests a stronger expansion with larger deviation from thermal equilibrium at higher energy. The kinetic freeze-out temperature at the same centrality shows a weak collision energy dependence for 7.7 to 39 GeV, while it decreases from 62.4 GeV to 5.02 TeV with an increase of nonequilibrium degree. A dependence of temperature and radial flow on nonequilibrium is observed and may be related to the bulk viscosity. Finally, we find that strange hadrons have a higher kinetic freeze-out temperature than that for light hadrons. The strange hadrons approach equilibrium more quickly from peripheral to central A+A collisions than nonstrange hadrons.

ACKNOWLEDGMENTS

We appreciate valuable discussions with Zhenyu Chen, Xiaofeng Luo, Nihar Ranjan Sahoo, Qinghua Xu, Chi Yang, and Qian Yang. This work was partly supported by the

National Natural Science Foundation of China under Grants No. 11890710, No. 11890713, and No. 11720101001. This work was also supported in part by the Office of Science of the U.S. Department of Energy.

APPENDIX

Extracted fit parameters and χ^2/nDoF are summarized in Tables III to VII for TBW model, in Table VIII to X for TBW4 model, and Table XI to XIII for BGBW model.

TABLE III. Extracted kinetic freeze-out parameters and χ^2/nDoF from TBW fits to identified particle transverse spectra in heavy ion collisions of different centralities at $\sqrt{s_{\rm NN}} = 7.7$ and 11.5 GeV. Results for charged pions, kaons, and protons have labels "(π, K, p)" behind their collision energy. All available hadrons including strange and multistrange particles are labeled as "(all)." We also fit the spectra separately for strangeness with label "(strange)" and nonstrange particles with label "(nonstrange)."

System	$\sqrt{s_{\rm NN}}$ (GeV)	Centrality	$\langle\beta\rangle$	T (MeV)	q	χ^2/nDoF
Au+Au	7.7 (π, K, p)	0–5%	0.436 ± 0.005	110 ± 2	$1.000^{+0.002}_{-0}$	113/133
		5–10%	0.428 ± 0.006	110 ± 2	$1.000^{+0.003}_{-0}$	106/134
		10–20%	0.39 ± 0.01	117 ± 3	1.006 ± 0.005	86/138
		20–30%	0.36 ± 0.01	117 ± 3	1.009 ± 0.005	129/136
		30–40%	0.34 ± 0.01	119 ± 3	1.008 ± 0.005	124/135
		40–50%	0.26 ± 0.03	117 ± 3	1.024 ± 0.006	110/125
		50–60%	0.21 ± 0.04	117 ± 3	1.026 ± 0.007	132/122
		60–70%	$0^{+0.07}_{-0}$	120 ± 3	1.034 ± 0.003	95/117
		70–80%	$0^{+0.06}_{-0}$	126 ± 3	1.021 ± 0.003	88/97
		0–80%	0.36 ± 0.02	111 ± 3	1.019 ± 0.008	48/90
Au+Au	7.7 (nonstrange)	0–5%	0.445 ± 0.006	108 ± 2	$1.000^{+0.003}_{-0}$	34/89
		5–10%	0.438 ± 0.006	109 ± 2	$1.000^{+0.005}_{-0}$	45/88
		10–20%	0.39 ± 0.01	116 ± 3	$1.005^{+0.006}_{-0}$	37/92
		20–30%	0.38 ± 0.01	115 ± 3	1.007 ± 0.006	31/90
		30–40%	0.35 ± 0.02	117 ± 3	1.009 ± 0.006	36/90
		40–60%	$0^{+0.06}_{-0}$	113 ± 3	1.049 ± 0.002	52/80
		60–80%	$0^{+0.07}_{-0}$	120 ± 3	1.032 ± 0.003	31/62
Au+Au	7.7 (strange)	0–5%	0.361 ± 0.01	133 ± 4	$1.0001^{+0.0002}_{-0.0001}$	178/80
		5–10%	0.358 ± 0.01	132 ± 4	$1.0001^{+0.0002}_{-0.0001}$	156/82
		10–20%	0.356 ± 0.009	131 ± 3	$1.0001^{+0.0002}_{-0.0001}$	160/82
		20–30%	0.351 ± 0.009	128 ± 3	$1.0001^{+0.0004}_{-0.0001}$	160/82
		30–40%	0.33 ± 0.01	130 ± 3	$1.000^{+0.001}_{-0}$	139/81
		40–60%	0.28 ± 0.02	133 ± 3	$1.002^{+0.003}_{-0.002}$	174/75
		60–80%	$0^{+0.06}_{-0}$	134 ± 3	1.022 ± 0.002	119/64
Au+Au	7.7 (all)	0–5%	0.407 ± 0.005	118 ± 2	1.0001 ± 0.0001	274/172
		5–10%	0.402 ± 0.005	118 ± 2	$1.0001^{+0.0002}_{-0.0001}$	251/173
		10–20%	0.378 ± 0.005	124 ± 2	$1.0001^{+0.0002}_{-0.0001}$	218/177
		20–30%	0.365 ± 0.005	124 ± 2	$1.0001^{+0.0003}_{-0.0001}$	216/175
		30–40%	0.349 ± 0.006	125 ± 2	$1.0001^{+0.0007}_{-0.0001}$	189/174
		40–60%	0.31 ± 0.01	127 ± 2	1.002 ± 0.002	229/158
		60–80%	0.20 ± 0.03	126 ± 2	1.012 ± 0.005	158/129
Au+Au	11.5 (π, K, p)	0–5%	0.423 ± 0.005	117 ± 2	$1.000^{+0.002}_{-0}$	104/142
		5–10%	0.416 ± 0.006	119 ± 2	$1.000^{+0.002}_{-0}$	79/145
		10–20%	0.399 ± 0.006	122 ± 2	$1.000^{+0.010}_{-0}$	92/145
		20–30%	0.35 ± 0.01	124 ± 3	1.012 ± 0.005	90/145
		30–40%	0.33 ± 0.02	122 ± 3	1.017 ± 0.005	109/144
		40–50%	$0^{+0.08}_{-0}$	126 ± 3	1.046 ± 0.002	114/140
		50–60%	$0^{+0.08}_{-0}$	124 ± 3	1.044 ± 0.002	96/138
		60–70%	$0^{+0.06}_{-0}$	128 ± 3	1.034 ± 0.002	108/124
		70–80%	$0^{+0.05}_{-0}$	125 ± 3	1.032 ± 0.003	117/120
		0–80%	0.37 ± 0.01	114 ± 3	1.019 ± 0.006	33/118

TABLE IV. Same as Table III, but for $\sqrt{s_{\rm NN}} = 11.5$ GeV (continued), 14.5 GeV, 17.3 GeV, and 19.6 GeV. The results at $\sqrt{s_{\rm NN}} = 17.3$ GeV are from Ref. [37].

System	$\sqrt{s_{\rm NN}}$ (GeV)	Centrality	$\langle\beta\rangle$	T (MeV)	q	χ^2/nDoF
Au+Au	11.5 (nonstrange)	0–5%	0.423 ± 0.005	118 ± 2	$1.00^{+0.01}_{-0}$	63/96
		5–10%	0.42 ± 0.01	119 ± 3	$1.00^{+0.03}_{-0}$	49/97
		10–20%	0.39 ± 0.01	121 ± 3	$1.004^{+0.007}_{-0.004}$	68/97
		20–30%	0.33 ± 0.02	119 ± 3	1.025 ± 0.007	56/97
		30–40%	0.29 ± 0.02	120 ± 3	1.026 ± 0.006	56/97
		40–60%	$0^{+0.08}_{-0}$	123 ± 3	1.047 ± 0.002	61/92
		60–80%	$0^{+0.06}_{-0}$	126 ± 3	1.034 ± 0.002	65/82
		0–80%	0.37 ± 0.02	113 ± 3	1.021 ± 0.008	21/82
Au+Au	11.5 (strange)	0–5%	0.387 ± 0.007	131 ± 3	$1.0001^{+0.0002}_{-0.0001}$	148/84
		5–10%	0.373 ± 0.008	135 ± 3	$1.0001^{+0.0004}_{-0.0001}$	154/86
		10–20%	0.376 ± 0.007	132 ± 2	$1.0001^{+0.0005}_{-0.0001}$	134/86
		20–30%	0.352 ± 0.007	138 ± 3	$1.000^{+0.001}_{-0}$	107/86
		30–40%	0.313 ± 0.009	147 ± 3	$1.000^{+0.007}_{-0}$	92/85
		40–60%	0.22 ± 0.02	146 ± 3	1.012 ± 0.003	126/84
		60–80%	$0^{+0.07}_{-0}$	145 ± 3	1.023 ± 0.002	132/73
Au+Au	11.5 (all)	0–5%	0.409 ± 0.004	122 ± 1	$1.0001^{+0.0002}_{-0.0001}$	228/183
		5–10%	0.402 ± 0.004	124 ± 2	$1.0001^{+0.0003}_{-0.0001}$	227/186
		10–20%	0.392 ± 0.004	126 ± 1	$1.0001^{+0.0006}_{-0.0001}$	214/186
		20–30%	0.368 ± 0.007	131 ± 2	$1.000^{+0.005}_{-0}$	185/186
		30–40%	0.340 ± 0.009	133 ± 2	1.003 ± 0.002	205/185
		40–60%	0.24 ± 0.01	136 ± 2	1.015 ± 0.002	228/179
		60–80%	$0^{+0.06}_{-0}$	134 ± 2	1.029 ± 0.001	240/158
Au+Au	14.5 (π, K, p)	0–5%	0.42 ± 0.01	118 ± 3	$1.006^{+0.007}_{-0.006}$	56/149
		5–10%	0.40 ± 0.01	119 ± 3	1.011 ± 0.007	58/149
		10–20%	0.38 ± 0.02	117 ± 3	1.016 ± 0.006	53/149
		20–30%	0.36 ± 0.02	118 ± 3	1.021 ± 0.006	33/149
		30–40%	0.31 ± 0.02	123 ± 3	1.024 ± 0.006	57/149
		40–50%	0.15 ± 0.06	115 ± 3	1.052 ± 0.007	83/143
		50–60%	0.15 ± 0.06	119 ± 3	1.045 ± 0.008	110/139
		60–70%	0.15 ± 0.07	119 ± 3	1.039 ± 0.008	79/131
		70–80%	$0^{+0.06}_{-0}$	126 ± 3	1.033 ± 0.003	93/127
Pb+Pb	17.3 (nonstrange) [37]	0–5%	0.442 ± 0.005	109 ± 1	1.015 ± 0.001	102/86
Pb+Pb	17.3 (strange) [37]	0–5%	0.420 ± 0.007	119 ± 4	1.009 ± 0.004	137/70
Pb+Pb	17.3 (all) [37]	0–5%	0.426 ± 0.004	113 ± 1	1.015 ± 0.001	267/159
Au+Au	19.6 (π, K, p)	0–5%	0.428 ± 0.009	112 ± 3	1.013 ± 0.005	52/146
		5–10%	0.41 ± 0.01	114 ± 3	1.016 ± 0.005	155/142
		10–20%	0.40 ± 0.01	117 ± 3	1.015 ± 0.005	73/142
		20–30%	0.34 ± 0.02	119 ± 3	1.028 ± 0.005	71/142
		30–40%	0.27 ± 0.02	124 ± 3	1.033 ± 0.006	84/143
		40–50%	0.20 ± 0.04	123 ± 3	1.041 ± 0.006	88/141
		50–60%	$0^{+0.05}_{-0}$	127 ± 2	1.047 ± 0.002	128/141
		60–70%	$0^{+0.04}_{-0}$	128 ± 3	1.042 ± 0.002	192/135
		70–80%	$0^{+0.04}_{-0}$	131 ± 3	1.033 ± 0.002	234/130
		0–80%	0.35 ± 0.01	111 ± 3	1.036 ± 0.006	33/127
Au+Au	19.6 (nonstrange)	0–5%	0.43 ± 0.01	111 ± 3	1.015 ± 0.007	40/96
		5–10%	0.40 ± 0.01	112 ± 3	1.022 ± 0.007	53/92
		10–20%	0.38 ± 0.02	112 ± 3	1.027 ± 0.007	36/92
		20–30%	0.32 ± 0.02	117 ± 3	1.034 ± 0.007	53/92
		30–40%	$0^{+0.07}_{-0}$	116 ± 3	1.065 ± 0.002	68/93
		40–60%	$0^{+0.06}_{-0}$	120 ± 3	1.057 ± 0.002	48/93
		60–80%	$0^{+0.04}_{-0}$	129 ± 3	1.040 ± 0.002	125/88
		0–80%	0.34 ± 0.02	110 ± 3	1.038 ± 0.007	24/86
Au+Au	19.6 (strange)	0–5%	0.404 ± 0.004	134 ± 2	1.0001 ± 0.0001	201/88
		5–10%	0.397 ± 0.004	136 ± 2	$1.0001^{+0.0003}_{-0.0001}$	181/88
		10–20%	0.388 ± 0.004	138 ± 2	$1.0001^{+0.0004}_{-0.0001}$	188/88
		20–30%	0.359 ± 0.007	145 ± 2	1.002 ± 0.002	182/88
		30–40%	0.319 ± 0.009	144 ± 2	1.009 ± 0.002	224/88
		40–60%	0.19 ± 0.02	146 ± 2	1.025 ± 0.003	271/86
		60–80%	$0^{+0.03}_{-0}$	141 ± 2	1.034 ± 0.001	265/79

TABLE V. Same as Table III, but for $\sqrt{s_{\rm NN}} = 19.6$ GeV (continued), 27 GeV, and 39 GeV.

System	$\sqrt{s_{\rm NN}}$ (GeV)	Centrality	$\langle\beta\rangle$	T (MeV)	q	χ^2/nDoF
Au+Au	19.6 (all)	0–5%	0.421 ± 0.003	126 ± 1	$1.0001^{+0.0002}_{-0.0001}$	293/187
		5–10%	0.414 ± 0.003	128 ± 1	$1.0001^{+0.0005}_{-0.0001}$	282/183
		10–20%	0.404 ± 0.003	131 ± 1	$1.000^{+0.001}_{-0}$	278/183
		20–30%	0.369 ± 0.006	135 ± 1	1.005 ± 0.002	312/183
		30–40%	0.324 ± 0.008	136 ± 1	1.013 ± 0.002	343/184
		40–60%	0.22 ± 0.02	138 ± 1	1.027 ± 0.002	374/182
		60–80%	$0^{+0.03}_{-0}$	134 ± 2	1.037 ± 0.001	411/170
Au+Au	27 (π, K, p)	0–5%	0.451 ± 0.009	114 ± 3	$1.004^{+0.006}_{-0.004}$	86/139
		5–10%	0.43 ± 0.01	112 ± 3	1.016 ± 0.006	66/140
		10–20%	0.40 ± 0.01	116 ± 3	1.019 ± 0.005	61/140
		20–30%	0.36 ± 0.01	116 ± 3	1.031 ± 0.005	54/140
		30–40%	0.30 ± 0.02	120 ± 3	1.038 ± 0.005	57/140
		40–50%	0.14 ± 0.06	120 ± 3	1.058 ± 0.006	48/140
		50–60%	$0^{+0.05}_{-0}$	126 ± 3	1.055 ± 0.002	102/140
		60–70%	$0^{+0.04}_{-0}$	130 ± 3	1.047 ± 0.002	162/140
		70–80%	$0^{+0.03}_{-0}$	133 ± 3	1.039 ± 0.002	267/138
		0–80%	0.38 ± 0.01	115 ± 3	1.027 ± 0.005	49/137
Au+Au	27 (nonstrange)	0–5%	0.43 ± 0.01	109 ± 3	1.021 ± 0.008	38/90
		5–10%	0.41 ± 0.01	108 ± 3	1.027 ± 0.007	39/90
		10–20%	0.39 ± 0.02	112 ± 3	1.029 ± 0.007	32/90
		20–30%	0.34 ± 0.02	113 ± 3	1.039 ± 0.007	29/90
		30–40%	0.26 ± 0.03	116 ± 3	1.050 ± 0.007	31/90
		40–60%	$0^{+0.04}_{-0}$	120 ± 3	1.061 ± 0.003	38/90
		60–80%	$0^{+0.03}_{-0}$	131 ± 3	1.044 ± 0.003	125/88
		0–80%	0.36 ± 0.02	110 ± 3	1.039 ± 0.007	22/88
Au+Au	27 (strange)	0–5%	0.419 ± 0.004	132 ± 2	$1.0001^{+0.0002}_{-0.0001}$	263/87
		5–10%	0.408 ± 0.004	136 ± 2	$1.0001^{+0.0002}_{-0.0001}$	199/88
		10–20%	0.396 ± 0.004	141 ± 2	$1.0001^{+0.0004}_{-0.0001}$	189/88
		20–30%	0.368 ± 0.006	148 ± 2	1.002 ± 0.002	177/88
		30–40%	0.31 ± 0.01	153 ± 2	1.011 ± 0.002	154/88
		40–60%	0.19 ± 0.03	155 ± 2	1.027 ± 0.003	201/88
		60–80%	$0^{+0.03}_{-0}$	145 ± 2	1.038 ± 0.001	253/88
Au+Au	27 (all)	0–5%	0.434 ± 0.003	125 ± 1	$1.0001^{+0.0002}_{-0.0001}$	350/180
		5–10%	0.426 ± 0.003	128 ± 1	$1.0001^{+0.0003}_{-0.0001}$	302/181
		10–20%	0.414 ± 0.003	132 ± 1	$1.0001^{+0.0009}_{-0.0001}$	290/181
		20–30%	0.379 ± 0.005	137 ± 1	1.006 ± 0.002	316/181
		30–40%	0.328 ± 0.008	141 ± 1	1.014 ± 0.002	302/181
		40–60%	0.22 ± 0.02	143 ± 1	1.029 ± 0.003	348/181
		60–80%	$0^{+0.03}_{-0}$	137 ± 1	1.042 ± 0.001	422/179
Au+Au	39 (π, K, p)	0–5%	0.463 ± 0.009	116 ± 3	$1.004^{+0.007}_{-0.004}$	57/140
		5–10%	0.44 ± 0.01	120 ± 3	1.010 ± 0.006	61/140
		10–20%	0.41 ± 0.01	114 ± 3	1.026 ± 0.006	48/140
		20–30%	0.36 ± 0.01	116 ± 3	1.036 ± 0.006	63/140
		30–40%	0.30 ± 0.02	120 ± 3	1.045 ± 0.006	53/140
		40–50%	0.18 ± 0.04	118 ± 3	1.062 ± 0.006	55/140
		50–60%	$0^{+0.05}_{-0}$	123 ± 3	1.063 ± 0.002	94/140
		60–70%	$0^{+0.04}_{-0}$	131 ± 3	1.054 ± 0.002	226/140
		70–80%	$0^{+0.03}_{-0}$	137 ± 3	1.045 ± 0.002	341/140
		0–80%	0.38 ± 0.01	117 ± 3	1.030 ± 0.006	46/140

TABLE VI. Same as Table III, but for $\sqrt{s_{\rm NN}} = 39$ GeV (continued), 62.4 GeV, and 200 GeV.

System	$\sqrt{s_{\rm NN}}$ (GeV)	Centrality	$\langle\beta\rangle$	T (MeV)	q	χ^2/nDoF
Au+Au	39 (nonstrange)	0–5%[a]	0.45 ± 0.01	111 ± 4	1.017 ± 0.009	39/90
		5–10%[a]	0.43 ± 0.01	116 ± 4	1.019 ± 0.009	45/90
		10–20%	0.39 ± 0.01	111 ± 3	1.036 ± 0.005	40/100
		20–30%[a]	0.35 ± 0.02	114 ± 4	1.042 ± 0.008	50/90
		30–40%[a]	$0^{+0.08}_{-0}$	112 ± 3	1.079 ± 0.003	49/90
		40–60%	$0^{+0.06}_{-0}$	120 ± 3	1.067 ± 0.005	43/100
		60–80%[a]	$0^{+0.03}_{-0}$	137 ± 3	1.045 ± 0.003	158/90
		0–80%[a]	0.37 ± 0.02	114 ± 3	1.039 ± 0.008	35/90
Au+Au	39 (strange)	0–5%	0.430 ± 0.007	134 ± 3	$1.000^{+0.003}_{-0}$	65/88
		5–10%	0.42 ± 0.01	134 ± 3	$1.001^{+0.003}_{-0.001}$	73/88
		10–20%	0.39 ± 0.01	143 ± 3	1.005 ± 0.003	85/88
		20–30%	0.36 ± 0.01	148 ± 3	1.009 ± 0.003	110/88
		30–40%	0.30 ± 0.02	153 ± 3	1.019 ± 0.003	93/88
		40–60%	$0^{+0.06}_{-0}$	154 ± 2	1.045 ± 0.001	166/88
		60–80%	$0^{+0.03}_{-0}$	149 ± 2	1.043 ± 0.002	221/88
Au+Au	39 (all)	0–5%[a]	0.454 ± 0.004	123 ± 2	$1.000^{+0.002}_{-0}$	131/181
		5–10%[a]	0.438 ± 0.007	126 ± 2	1.003 ± 0.003	133/181
		10–20%	0.408 ± 0.007	129 ± 2	1.012 ± 0.003	190/191
		20–30%[a]	0.382 ± 0.008	134 ± 2	1.013 ± 0.002	234/181
		30–40%[a]	0.32 ± 0.01	138 ± 2	1.023 ± 0.002	214/181
		40–60%	0.14 ± 0.04	141 ± 2	1.046 ± 0.004	309/191
		60–80%[a]	$0^{+0.02}_{-0}$	138 ± 2	1.048 ± 0.001	464/181
Au+Au	62.4 (π, K, p)	0–10%	0.47 ± 0.01	124 ± 3	$1.002^{+0.006}_{-0.002}$	104/65
		10–20%	0.44 ± 0.01	124 ± 3	1.015 ± 0.006	96/65
		20–40%	0.39 ± 0.02	125 ± 4	1.028 ± 0.005	85/65
		40–80%	0.18 ± 0.05	128 ± 4	1.059 ± 0.006	91/65
Au+Au	62.4 (nonstrange)	0–20%	0.43 ± 0.01	121 ± 3	1.022 ± 0.005	93/57
		20–40%	0.36 ± 0.02	121 ± 3	1.039 ± 0.004	69/57
		40–80%[a]	$0^{+0.14}_{-0}$	124 ± 4	1.068 ± 0.007	73/47
Au+Au	62.4 (strange)	0–20%	0.34 ± 0.02	190 ± 10	$1.000^{+0.001}_{-0}$	50/73
		20–40%	0.35 ± 0.02	182 ± 8	$1.000^{+0.003}_{-0}$	43/73
		40–80%	0.23 ± 0.07	169 ± 7	1.03 ± 0.01	70/67
Au+Au	62.4 (all)	0–20%	0.443 ± 0.009	137 ± 3	$1.001^{+0.006}_{-0.001}$	215/133
		20–40%	0.38 ± 0.01	136 ± 3	1.021 ± 0.004	181/133
		40–80%[a]	0.20 ± 0.04	139 ± 3	1.048 ± 0.006	185/117
Au+Au	200 (π, K, p)	0–10%[b]	0.45 ± 0.01	111 ± 3	1.039 ± 0.004	105/79
		10–20%	0.44 ± 0.01	113 ± 3	1.039 ± 0.005	98/79
		20–40%	0.36 ± 0.02	115 ± 3	1.057 ± 0.004	112/81
		40–60%	0.22 ± 0.04	117 ± 3	1.075 ± 0.004	87/81
		60–80%	$0^{+0.04}_{-0}$	111 ± 3	1.088 ± 0.002	79/81
Au+Au	200 (nonstrange)	0–10%[b]	0.43 ± 0.01	110 ± 3	1.044 ± 0.004	73/61
		10–20%	0.42 ± 0.01	112 ± 3	1.047 ± 0.005	67/59
		20–40%	0.33 ± 0.02	114 ± 3	1.064 ± 0.004	75/61
		40–60%	0.16 ± 0.05	115 ± 3	1.081 ± 0.004	68/61
		60–80%	$0^{+0.04}_{-0}$	110 ± 3	1.088 ± 0.002	74/61
Au+Au	200 (strange)	0–10%[c]	0.43 ± 0.01	133 ± 4	1.027 ± 0.005	92/111
		10–20%[d]	0.43 ± 0.01	131 ± 4	1.028 ± 0.005	112/111
		20–40%	0.39 ± 0.01	131 ± 3	1.037 ± 0.005	171/113
		40–60%	0.22 ± 0.03	110 ± 3	1.081 ± 0.004	165/113
		60–80%[e]	0.31 ± 0.04	110 ± 10	1.059 ± 0.007	54/59

[a]Lack of measurements of π^0 at this centrality class [47].
[b]The measurements of $\pi^{\pm}$, p, and $\bar{p}$ for centrality 0–12% [43] are used as 0–10%.
[c]The measurements of Λ, $\bar{\Lambda}$, Ξ^+, Ξ^-, and Ω for centrality 0–5% [49] are used as 0–10%.
[d]Lack of measurements of Ω at this centrality class [49].
[e]Lack of measurements of Ω [49] and intermediate p_T $K^{\pm}$ [48] at this centrality class.

TABLE VII. Same as Table III, but for $\sqrt{s_{\rm NN}} = 200$ GeV (continued), 2760 GeV, and 5020 GeV. Previous studies of 200 GeV from Refs. [10,37] are also listed. The difference between our results at 200 GeV from previous ones is due to the fact that more data points at $2 \leqslant p_T \leqslant 3$ GeV/c are available now and are thus used in fitting, mainly $K^{\pm}$ data from PHENIX [48] which provide better constraint on q, while data for $K^{\pm}$ used in Ref. [10] are only at $p_T \leqslant 0.8$ GeV/c and data for $K^{\pm}$ used in Ref. [37] are only at $p_T \leqslant 2$ GeV/c.

System	$\sqrt{s_{\rm NN}}$ (GeV)	Centrality	$\langle\beta\rangle$	T (MeV)	q	χ^2/nDoF
Au+Au	200 (all)	0–10%[a]	0.435 ± 0.007	118 ± 2	1.036 ± 0.003	186/175
		10–20%[b]	0.436 ± 0.007	118 ± 2	1.036 ± 0.003	198/173
		20–40%	0.378 ± 0.009	120 ± 2	1.049 ± 0.003	278/177
		40–60%	0.23 ± 0.02	112 ± 2	1.078 ± 0.003	237/177
		60–80%[c]	$0^{+0.04}_{-0}$	113 ± 3	1.086 ± 0.002	139/123
Au+Au	200 (all) [10]	0–10%	0.470 ± 0.009	122 ± 2	1.018 ± 0.005	130/125
		10–20%	0.475 ± 0.008	122 ± 2	1.015 ± 0.005	119/127
		20–40%	0.441 ± 0.009	124 ± 2	1.024 ± 0.004	159/127
		40–60%	0.282 ± 0.017	119 ± 2	1.066 ± 0.003	165/135
		60–80%	$0^{+0.05}_{-0}$	114 ± 3	1.086 ± 0.002	138/123
Au+Au	200 (all) [37]	0–10%	0.472 ± 0.009	122 ± 3	1.017 ± 0.006	140/155
Pb+Pb	2760 (π, K, p)	0–5%	0.591 ± 0.003	91 ± 2	1.024 ± 0.005	247/213
		5–10%	0.587 ± 0.003	91 ± 2	1.029 ± 0.005	247/213
		10–20%	0.580 ± 0.003	92 ± 2	1.035 ± 0.005	230/213
		20–30%	0.563 ± 0.004	92 ± 2	1.046 ± 0.005	207/213
		30–40%	0.535 ± 0.005	92 ± 2	1.061 ± 0.004	201/213
		40–50%	0.493 ± 0.005	90 ± 2	1.078 ± 0.003	185/213
		50–60%	0.437 ± 0.007	90 ± 2	1.091 ± 0.003	196/213
		60–70%	0.35 ± 0.01	91 ± 2	1.104 ± 0.002	244/213
		70–80%	0.23 ± 0.02	91 ± 2	1.116 ± 0.002	299/213
		80–90%	$0^{+0.01}_{-0}$	90 ± 2	1.122 ± 0.001	344/213
Pb+Pb	2760 (nonstrange)	0–10%	0.587 ± 0.003	88 ± 2	1.034 ± 0.005	209/143
		10–20%	0.576 ± 0.004	89 ± 2	1.042 ± 0.005	201/143
		20–40%	0.548 ± 0.005	91 ± 2	1.057 ± 0.005	189/143
		40–60%	0.463 ± 0.007	90 ± 2	1.086 ± 0.003	168/143
		60–80%	0.28 ± 0.01	91 ± 2	1.112 ± 0.003	198/143
		80–90%	$0^{+0.01}_{-0}$	90 ± 2	1.120 ± 0.001	225/143
Pb+Pb	2760 (strange)	0–10%	0.561 ± 0.003	133 ± 3	$1.000^{+0.001}_{-0}$	125/139
		10–20%	0.550 ± 0.003	143 ± 3	$1.000^{+0.002}_{-0}$	74/139
		20–40%	0.519 ± 0.008	157 ± 5	$1.006^{+0.008}_{-0.006}$	61/139
		40–60%	0.43 ± 0.01	148 ± 5	1.047 ± 0.006	53/139
		60–80%	0.25 ± 0.03	139 ± 5	1.088 ± 0.005	72/137
Pb+Pb	2760 (all)	0–10%	0.578 ± 0.003	99 ± 2	1.024 ± 0.004	517/285
		10–20%	0.566 ± 0.003	100 ± 2	1.033 ± 0.004	467/285
		20–40%	0.534 ± 0.004	101 ± 2	1.050 ± 0.004	470/285
		40–60%	0.457 ± 0.005	99 ± 2	1.078 ± 0.003	373/285
		60–80%	0.31 ± 0.01	96 ± 2	1.106 ± 0.002	396/283
Pb+Pb	5020 (π, K, p)	0–5%	0.605 ± 0.002	93 ± 2	1.021 ± 0.005	316/90
		5–10%	0.602 ± 0.003	91 ± 2	1.030 ± 0.005	303/90
		10–20%	0.596 ± 0.003	93 ± 2	1.031 ± 0.005	317/90
		20–30%	0.581 ± 0.003	94 ± 2	1.042 ± 0.004	268/90
		30–40%	0.557 ± 0.003	93 ± 2	1.058 ± 0.004	217/90
		40–50%	0.517 ± 0.004	92 ± 2	1.076 ± 0.003	189/90
		50–60%	0.459 ± 0.005	92 ± 2	1.092 ± 0.003	192/90
		60–70%	0.383 ± 0.009	89 ± 2	1.109 ± 0.003	177/90
		70–80%	0.26 ± 0.02	88 ± 2	1.123 ± 0.003	189/90
		80–90%	$0^{+0.01}_{-0}$	88 ± 2	1.131 ± 0.003	174/90

[a]The measurements of $\pi^{\pm}$, p, and $\bar{p}$ for centrality 0–12% [43] are used as 0–10%. Λ, $\bar{\Lambda}$, Ξ^{+}, Ξ^{-}, and Ω for centrality 0–5% [49] are used as 0–10%.

[b]Lack of measurements of Ω at this centrality class [49].

[c]Lack of measurements of Ω [49] and intermediate p_T $K^{\pm}$ [48] at this centrality class.

TABLE VIII. Extracted kinetic freeze-out parameters and $\chi^2/n\mathrm{DoF}$ from TBW4 fits to identified particle transverse spectra in heavy ion collisions of different centralities at $\sqrt{s_{\mathrm{NN}}} = 7.7$, 11.5, 14.5, and 19.6 GeV. Results for charged pions, kaons, and protons have labels "(π, K, p)" behind their collision energy. All available hadrons including strange and multistrange particles are labeled as "(all)."

System	$\sqrt{s_{\mathrm{NN}}}$ (GeV)	Centrality	$\langle\beta\rangle$	T (MeV)	q_M	q_B	$\chi^2/n\mathrm{DoF}$
Au+Au	7.7 (π, K, p)	0−5%	0.431 ± 0.008	111 ± 2	$1.000^{+0.002}_{-0}$	1.003 ± 0.003	112/132
		5−10%	0.418 ± 0.009	113 ± 3	$1.000^{+0.003}_{-0}$	1.005 ± 0.003	103/133
		10−20%	0.39 ± 0.01	117 ± 4	1.006 ± 0.005	1.006 ± 0.006	86/137
		20−30%	0.34 ± 0.02	123 ± 4	1.008 ± 0.005	1.015 ± 0.006	120/135
		30−40%	0.32 ± 0.02	125 ± 4	1.006 ± 0.005	1.013 ± 0.006	118/134
		40−50%	0.26 ± 0.03	116 ± 4	1.024 ± 0.006	1.023 ± 0.006	110/124
		50−60%	0.17 ± 0.08	121 ± 4	1.03 ± 0.01	1.03 ± 0.01	130/121
		60−70%	$0^{+0.095}_{-0}$	121 ± 4	1.033 ± 0.004	1.034 ± 0.003	95/116
		70−80%	$0^{+0.095}_{-0}$	116 ± 4	1.032 ± 0.005	1.025 ± 0.003	80/96
		0−80%	0.37 ± 0.02	105 ± 5	1.026 ± 0.009	1.020 ± 0.008	46/89
Au+Au	7.7 (all)	0−5%	0.426 ± 0.005	105 ± 2	1.010 ± 0.002	1.0001 ± 0.0002	234/171
		5−10%	0.421 ± 0.005	106 ± 2	1.009 ± 0.002	1.0001 ± 0.0002	218/172
		10−20%	0.399 ± 0.005	112 ± 2	1.008 ± 0.001	1.0001 ± 0.0002	186/176
		20−30%	0.377 ± 0.006	117 ± 3	1.004 ± 0.001	$1.0001^{+0.0003}_{-0.0001}$	207/174
		30−40%	0.362 ± 0.007	118 ± 3	1.004 ± 0.001	$1.000^{+0.001}_{-0}$	180/173
		40−60%	0.32 ± 0.01	117 ± 3	1.009 ± 0.003	1.003 ± 0.002	210/157
		60−80%	0.24 ± 0.02	112 ± 3	1.022 ± 0.004	1.011 ± 0.004	122/128
Au+Au	11.5 (π, K, p)	0−5%	0.429 ± 0.006	112 ± 3	1.005 ± 0.002	$1.000^{+0.001}_{-0}$	100/141
		5−10%	0.417 ± 0.006	117 ± 3	$1.001^{+0.002}_{-0.001}$	$1.000^{+0.002}_{-0}$	79/144
		10−20%	0.404 ± 0.006	118 ± 3	1.004 ± 0.002	$1.000^{+0.003}_{-0}$	88/144
		20−30%	0.36 ± 0.02	121 ± 3	1.012 ± 0.005	1.009 ± 0.006	88/144
		30−40%	0.37 ± 0.01	112 ± 3	1.019 ± 0.005	1.008 ± 0.005	90/143
		40−50%	0.24 ± 0.03	121 ± 3	1.031 ± 0.005	1.025 ± 0.006	104/139
		50−60%	0.24 ± 0.03	116 ± 3	1.032 ± 0.005	1.023 ± 0.005	79/137
		60−70%	$0^{+0.14}_{-0}$	118 ± 3	1.044 ± 0.003	1.037 ± 0.002	86/123
		70−80%	$0^{+0.08}_{-0}$	116 ± 3	1.041 ± 0.003	1.034 ± 0.003	101/119
		0−80%	0.38 ± 0.01	109 ± 4	1.022 ± 0.006	1.017 ± 0.006	30/117
Au+Au	11.5 (all)	0−5%	0.433 ± 0.004	107 ± 2	1.010 ± 0.001	$1.0001^{+0.0002}_{-0.0001}$	169/182
		5−10%	0.427 ± 0.004	108 ± 2	1.011 ± 0.001	$1.0001^{+0.0003}_{-0.0001}$	163/185
		10−20%	0.418 ± 0.004	110 ± 2	1.010 ± 0.001	$1.0001^{+0.0009}_{-0.0001}$	152/185
		20−30%	0.394 ± 0.007	116 ± 2	1.010 ± 0.002	$1.001^{+0.002}_{-0.001}$	133/185
		30−40%	0.376 ± 0.007	113 ± 2	1.015 ± 0.002	1.004 ± 0.002	124/184
		40−60%	0.30 ± 0.01	118 ± 3	1.022 ± 0.002	1.013 ± 0.002	154/178
		60−80%	0.25 ± 0.02	113 ± 3	1.028 ± 0.003	1.014 ± 0.003	131/157
Au+Au	14.5 (π, K, p)	0−5%	0.43 ± 0.02	116 ± 4	$1.005^{+0.007}_{-0.005}$	$1.002^{+0.008}_{-0.002}$	55/148
		5−10%	0.41 ± 0.02	117 ± 4	1.010 ± 0.007	1.008 ± 0.008	57/148
		10−20%	0.39 ± 0.02	116 ± 4	1.016 ± 0.006	1.015 ± 0.007	53/148
		20−30%	0.39 ± 0.02	114 ± 4	1.020 ± 0.006	1.015 ± 0.007	30/148
		30−40%	0.32 ± 0.03	122 ± 4	1.023 ± 0.006	1.022 ± 0.007	57/148
		40−50%	0.1 ± 0.1	116 ± 4	1.054 ± 0.009	1.055 ± 0.011	83/142
		50−60%	0.27 ± 0.03	111 ± 4	1.037 ± 0.006	1.028 ± 0.007	99/138
		60−70%	0.18 ± 0.07	118 ± 4	1.036 ± 0.008	1.03 ± 0.01	79/130
		70−80%	0.26 ± 0.03	111 ± 4	1.026 ± 0.006	1.012 ± 0.007	68/126
Au+Au	19.6 (π, K, p)	0−5%	0.44 ± 0.01	110 ± 3	1.013 ± 0.005	1.010 ± 0.006	51/145
		5−10%	0.42 ± 0.01	110 ± 3	1.016 ± 0.005	1.010 ± 0.006	70/141
		10−20%	0.40 ± 0.01	116 ± 3	1.015 ± 0.005	1.015 ± 0.006	73/141
		20−30%	0.36 ± 0.02	114 ± 3	1.028 ± 0.005	1.022 ± 0.005	65/141
		30−40%	0.30 ± 0.02	120 ± 3	1.031 ± 0.005	1.027 ± 0.006	81/142
		40−50%	0.15 ± 0.09	125 ± 3	1.045 ± 0.009	1.05 ± 0.01	87/140
		50−60%	$0^{+0.08}_{-0}$	120 ± 3	1.053 ± 0.002	1.047 ± 0.002	106/140
		60−70%	$0^{+0.05}_{-0}$	115 ± 3	1.055 ± 0.003	1.044 ± 0.002	135/134
		70−80%	$0^{+0.05}_{-0}$	113 ± 3	1.053 ± 0.003	1.039 ± 0.002	125/129
		0−80%	0.36 ± 0.02	108 ± 4	1.036 ± 0.006	1.032 ± 0.006	31/126
Au+Au	19.6 (all)	0−5%	0.453 ± 0.003	105 ± 2	1.013 ± 0.001	$1.0001^{+0.0002}_{-0.0001}$	162/186
		5−10%	0.446 ± 0.004	107 ± 2	1.013 ± 0.002	$1.000^{+0.002}_{-0}$	158/182
		10−20%	0.431 ± 0.004	110 ± 2	1.015 ± 0.002	1.003 ± 0.002	165/182
		20−30%	0.406 ± 0.005	109 ± 2	1.022 ± 0.002	1.009 ± 0.001	146/182
		30−40%	0.370 ± 0.006	110 ± 2	1.027 ± 0.002	1.015 ± 0.002	198/183
		40−60%	0.305 ± 0.009	113 ± 2	1.035 ± 0.002	1.023 ± 0.002	230/181
		60−80%	0.17 ± 0.03	113 ± 2	1.048 ± 0.003	1.034 ± 0.003	197/169

TABLE IX. Same as Table VIII, but for $\sqrt{s_{\rm NN}} = 27$, 39, 62.4, and 200 GeV.

System	$\sqrt{s_{\rm NN}}$ (GeV)	Centrality	$\langle\beta\rangle$	T (MeV)	q_M	q_B	χ^2/nDoF
Au+Au	27 (π, K, p)	0–5%	0.45 ± 0.01	114 ± 3	$1.004^{+0.006}_{-0.004}$	1.004 ± 0.007	86/138
		5–10%	0.43 ± 0.01	111 ± 3	1.016 ± 0.006	1.013 ± 0.006	65/139
		10–20%	0.41 ± 0.01	114 ± 3	1.019 ± 0.005	1.017 ± 0.006	61/139
		20–30%	0.38 ± 0.02	112 ± 3	1.031 ± 0.005	1.026 ± 0.006	50/139
		30–40%	0.34 ± 0.02	112 ± 3	1.037 ± 0.005	1.028 ± 0.005	45/139
		40–50%	0.25 ± 0.03	114 ± 3	1.051 ± 0.005	1.043 ± 0.006	36/139
		50–60%	0.19 ± 0.05	114 ± 3	1.055 ± 0.006	1.044 ± 0.007	47/139
		60–70%	$0^{+0.06}_{-0}$	114 ± 3	1.063 ± 0.002	1.049 ± 0.002	57/139
		70–80%	$0^{+0.05}_{-0}$	113 ± 3	1.060 ± 0.002	1.042 ± 0.002	83/137
		0–80%	0.39 ± 0.01	113 ± 3	1.026 ± 0.005	1.024 ± 0.006	48/136
Au+Au	27 (all)	0–5%	0.464 ± 0.003	104 ± 2	1.014 ± 0.001	$1.0001^{+0.0003}_{-0.0001}$	211/179
		5–10%	0.458 ± 0.003	105 ± 2	1.014 ± 0.001	$1.000^{+0.002}_{-0}$	158/180
		10–20%	0.443 ± 0.004	108 ± 2	1.017 ± 0.002	1.004 ± 0.002	139/180
		20–30%	0.418 ± 0.004	109 ± 2	1.024 ± 0.002	1.010 ± 0.001	127/180
		30–40%	0.385 ± 0.006	110 ± 2	1.030 ± 0.002	1.016 ± 0.001	101/180
		40–60%	0.329 ± 0.008	110 ± 2	1.040 ± 0.002	1.024 ± 0.002	100/180
		60–80%	0.16 ± 0.03	115 ± 2	1.055 ± 0.002	1.040 ± 0.003	124/178
Au+Au	39 (π, K, p)	0–5%	0.47 ± 0.01	115 ± 3	$1.004^{+0.007}_{-0.004}$	$1.003^{+0.008}_{-0.003}$	58/139
		5–10%	0.45 ± 0.01	117 ± 4	1.009 ± 0.006	$1.005^{+0.007}_{-0.005}$	58/139
		10–20%	0.42 ± 0.01	110 ± 3	1.026 ± 0.006	1.020 ± 0.006	43/139
		20–30%	0.39 ± 0.01	109 ± 3	1.036 ± 0.005	1.027 ± 0.006	52/139
		30–40%	0.36 ± 0.02	110 ± 3	1.043 ± 0.005	1.032 ± 0.006	33/139
		40–50%	0.27 ± 0.03	111 ± 3	1.056 ± 0.005	1.048 ± 0.006	43/139
		50–60%	0.16 ± 0.06	112 ± 3	1.066 ± 0.006	1.055 ± 0.007	55/139
		60–70%	0.20 ± 0.04	106 ± 3	1.067 ± 0.005	1.045 ± 0.006	41/139
		70–80%	$0^{+0.1}_{-0}$	108 ± 3	1.074 ± 0.003	1.051 ± 0.002	59/139
		0–80%	0.40 ± 0.01	111 ± 3	1.030 ± 0.005	1.023 ± 0.006	40/139
Au+Au	39 (all)	0–5%[a]	0.470 ± 0.004	109 ± 2	1.011 ± 0.002	$1.000^{+0.001}_{-0}$	90/180
		5–10%[a]	0.458 ± 0.006	111 ± 3	1.014 ± 0.003	$1.002^{+0.003}_{-0.002}$	86/180
		10–20%	0.447 ± 0.006	107 ± 2	1.023 ± 0.002	1.008 ± 0.002	83/190
		20–30%[a]	0.427 ± 0.006	107 ± 2	1.029 ± 0.003	1.012 ± 0.002	88/180
		30–40%[a]	0.389 ± 0.007	109 ± 2	1.036 ± 0.002	1.020 ± 0.002	58/180
		40–60%	0.33 ± 0.01	109 ± 2	1.046 ± 0.002	1.029 ± 0.002	90/190
		60–80%[a]	0.21 ± 0.02	110 ± 2	1.060 ± 0.002	1.039 ± 0.003	75/180
Au+Au	62.4 (π, K, p)	0–10%	0.522 ± 0.005	85 ± 4	1.035 ± 0.004	$1.000^{+0.002}_{-0}$	26/64
		10–20%	0.512 ± 0.009	89 ± 5	1.035 ± 0.006	$1.002^{+0.005}_{-0.002}$	34/64
		20–40%	0.48 ± 0.01	88 ± 5	1.047 ± 0.005	1.016 ± 0.005	19/64
		40–80%	0.40 ± 0.02	91 ± 5	1.061 ± 0.004	1.033 ± 0.004	31/64
Au+Au	62.4 (all)	0–20%	0.487 ± 0.005	104 ± 3	1.024 ± 0.002	$1.000^{+0.001}_{-0}$	113/132
		20–40%	0.451 ± 0.009	106 ± 4	1.034 ± 0.004	1.011 ± 0.004	84/132
		40–80%[a]	0.38 ± 0.01	101 ± 4	1.056 ± 0.004	1.030 ± 0.004	64/116
Au+Au	200 (π, K, p)	0–10%[b]	0.544 ± 0.008	79 ± 4	1.045 ± 0.004	1.006 ± 0.005	24/78
		10–20%	0.534 ± 0.009	80 ± 4	1.050 ± 0.004	1.012 ± 0.005	24/78
		20–40%	0.51 ± 0.01	78 ± 4	1.063 ± 0.004	1.025 ± 0.005	24/80
		40–60%	0.44 ± 0.02	83 ± 4	1.074 ± 0.003	1.043 ± 0.005	33/80
		60–80%	0.31 ± 0.04	88 ± 5	1.088 ± 0.003	1.062 ± 0.005	21/80
Au+Au	200 (all)	0–10%[c]	0.458 ± 0.006	104 ± 3	1.044 ± 0.003	1.032 ± 0.003	140/174
		10–20%[d]	0.458 ± 0.006	101 ± 3	1.048 ± 0.003	1.033 ± 0.003	119/172
		20–40%	0.425 ± 0.007	95 ± 2	1.063 ± 0.003	1.044 ± 0.003	136/176
		40–60%	0.30 ± 0.01	96 ± 3	1.083 ± 0.002	1.070 ± 0.003	173/176
		60–80%[e]	0.28 ± 0.02	92 ± 3	1.088 ± 0.003	1.068 ± 0.004	56/122

[a]Lack of measurements of π^0 at this centrality class [47].
[b]The measurements of $\pi^\pm$, p, and $\bar{p}$ for centrality 0–12% [43] are used as 0–10%.
[c]The measurements of $\pi^\pm$, p, and $\bar{p}$ for centrality 0–12% [43] are used as 0–10%. Λ, $\bar{\Lambda}$, Ξ^+, Ξ^-, and Ω for centrality 0–5% [49] are used as 0–10%.
[d]Lack of measurements of Ω at this centrality class [49].
[e]Lack of measurements of Ω [49] and intermediate p_T $K^\pm$ [48] at this centrality class.

TABLE X. Same as Table VIII, but for $\sqrt{s_{\rm NN}} = 2.76$ and 5.02 TeV.

System	$\sqrt{s_{\rm NN}}$ (TeV)	Centrality	$\langle\beta\rangle$	T (MeV)	q_M	q_B	χ^2/nDoF
Pb+Pb	2.76 (π, K, p)	0−5%	0.590 ± 0.004	92 ± 2	1.024 ± 0.005	1.026 ± 0.006	246/212
		5−10%	0.588 ± 0.004	91 ± 2	1.030 ± 0.005	1.028 ± 0.006	247/212
		10−20%	0.584 ± 0.004	90 ± 2	1.035 ± 0.005	1.029 ± 0.006	225/212
		20−30%	0.574 ± 0.005	88 ± 2	1.046 ± 0.005	1.034 ± 0.006	191/212
		30−40%	0.557 ± 0.005	84 ± 2	1.061 ± 0.004	1.044 ± 0.005	162/212
		40−50%	0.525 ± 0.006	80 ± 2	1.079 ± 0.003	1.060 ± 0.004	127/212
		50−60%	0.485 ± 0.007	78 ± 2	1.094 ± 0.003	1.073 ± 0.004	117/212
		60−70%	0.441 ± 0.008	74 ± 2	1.107 ± 0.002	1.082 ± 0.003	105/212
		70−80%	0.40 ± 0.01	71 ± 2	1.117 ± 0.002	1.088 ± 0.003	94/212
		80−90%	0.33 ± 0.02	69 ± 2	1.124 ± 0.002	1.093 ± 0.003	85/212
Pb+Pb	2.76 (all)	0−10%	0.577 ± 0.003	100 ± 2	1.025 ± 0.004	1.025 ± 0.005	513/284
		10−20%	0.570 ± 0.004	98 ± 2	1.034 ± 0.004	1.028 ± 0.005	462/284
		20−40%	0.549 ± 0.004	94 ± 2	1.051 ± 0.004	1.039 ± 0.004	439/284
		40−60%	0.498 ± 0.005	86 ± 2	1.081 ± 0.003	1.062 ± 0.003	273/284
		60−80%	0.421 ± 0.008	77 ± 2	1.108 ± 0.002	1.082 ± 0.003	162/282
Pb+Pb	5.02 (π, K, p)	0−5%	0.596 ± 0.003	99 ± 2	1.021 ± 0.005	1.041 ± 0.006	274/89
		5−10%	0.596 ± 0.003	95 ± 2	1.028 ± 0.005	1.040 ± 0.005	286/89
		10−20%	0.591 ± 0.003	96 ± 2	1.031 ± 0.005	1.040 ± 0.005	306/89
		20−30%	0.580 ± 0.004	95 ± 2	1.042 ± 0.004	1.044 ± 0.005	267/89
		30−40%	0.565 ± 0.004	91 ± 2	1.058 ± 0.004	1.050 ± 0.004	207/89
		40−50%	0.535 ± 0.005	86 ± 2	1.077 ± 0.003	1.064 ± 0.004	156/89
		50−60%	0.492 ± 0.006	83 ± 2	1.094 ± 0.003	1.078 ± 0.003	128/89
		60−70%	0.447 ± 0.008	75 ± 2	1.112 ± 0.003	1.089 ± 0.003	69/89
		70−80%	0.38 ± 0.01	73 ± 2	1.124 ± 0.002	1.099 ± 0.003	54/89
		80−90%	0.32 ± 0.02	72 ± 2	1.130 ± 0.002	1.104 ± 0.003	51/89

TABLE XI. Extracted kinetic freeze-out parameters and $\chi^2/n\mathrm{DoF}$ from BGBW fits to identified particle transverse spectra in heavy ion collisions of different centralities at $\sqrt{s_{\mathrm{NN}}} = 7.7$, 11.5, 14.5, and 19.6 GeV. Results for charged pions, kaons, and protons have labels "(π, K, p)" behind their collision energy. All available hadrons including strange and multistrange particles are labeled as "(all)."

System	$\sqrt{s_{\mathrm{NN}}}$ (GeV)	Centrality	$\langle\beta\rangle$	T (MeV)	$\chi^2/n\mathrm{DoF}$
Au+Au	7.7 (π, K, p)	0−5%	0.437 ± 0.005	110 ± 2	114/134
		5−10%	0.428 ± 0.006	110 ± 2	107/135
		10−20%	0.395 ± 0.007	119 ± 2	87/139
		20−30%	0.378 ± 0.007	120 ± 2	132/137
		30−40%	0.357 ± 0.008	122 ± 2	127/136
		40−50%	0.328 ± 0.009	124 ± 2	127/126
		50−60%	0.30 ± 0.01	123 ± 2	149/123
		60−70%	0.26 ± 0.01	126 ± 2	107/118
		70−80%	0.19 ± 0.02	131 ± 2	93/98
		0−80%	0.401 ± 0.008	116 ± 2	53/91
Au+Au	7.7 (all)	0−5%	0.407 ± 0.005	118 ± 2	274/173
		5−10%	0.403 ± 0.005	118 ± 2	251/174
		10−20%	0.378 ± 0.005	124 ± 2	218/178
		20−30%	0.365 ± 0.005	124 ± 2	217/176
		30−40%	0.349 ± 0.006	125 ± 2	190/175
		40−60%	0.312 ± 0.006	127 ± 2	230/159
		60−80%	0.259 ± 0.009	127 ± 2	165/130
Au+Au	11.5 (π, K, p)	0−5%	0.423 ± 0.005	118 ± 2	105/143
		5−10%	0.416 ± 0.005	119 ± 2	80/146
		10−20%	0.398 ± 0.006	122 ± 2	92/146
		20−30%	0.375 ± 0.007	128 ± 2	95/146
		30−40%	0.361 ± 0.007	129 ± 2	121/145
		40−50%	0.302 ± 0.009	138 ± 2	153/141
		50−60%	0.291 ± 0.009	136 ± 2	139/139
		60−70%	0.25 ± 0.01	137 ± 2	130/125
		70−80%	0.23 ± 0.01	136 ± 2	145/121
		0−80%	0.403 ± 0.007	120 ± 2	40/119
Au+Au	11.5 (all)	0−5%	0.410 ± 0.004	122 ± 1	228/184
		5−10%	0.402 ± 0.004	124 ± 2	228/187
		10−20%	0.392 ± 0.004	126 ± 1	215/187
		20−30%	0.369 ± 0.005	131 ± 2	186/187
		30−40%	0.350 ± 0.005	133 ± 2	207/186
		40−60%	0.307 ± 0.006	138 ± 2	276/180
		60−80%	0.259 ± 0.008	137 ± 2	276/159
Au+Au	14.5 (π, K, p)	0−5%	0.427 ± 0.006	120 ± 2	58/150
		5−10%	0.416 ± 0.007	123 ± 2	61/150
		10−20%	0.415 ± 0.007	123 ± 2	59/150
		20−30%	0.403 ± 0.007	125 ± 2	44/150
		30−40%	0.373 ± 0.008	130 ± 2	71/150
		40−50%	0.344 ± 0.009	133 ± 3	139/144
		50−60%	0.32 ± 0.01	134 ± 3	149/140
		60−70%	0.31 ± 0.01	130 ± 3	108/132
		70−80%	0.26 ± 0.01	133 ± 3	107/128
Au+Au	19.6 (π, K, p)	0−5%	0.446 ± 0.005	117 ± 2	57/147
		5−10%	0.433 ± 0.005	120 ± 2	82/143
		10−20%	0.421 ± 0.006	122 ± 2	82/143
		20−30%	0.393 ± 0.006	129 ± 2	99/143
		30−40%	0.357 ± 0.007	135 ± 2	120/144
		40−50%	0.338 ± 0.008	136 ± 2	143/142
		50−60%	0.289 ± 0.008	144 ± 2	214/142
		60−70%	0.257 ± 0.009	145 ± 2	279/136
		70−80%	0.22 ± 0.01	146 ± 2	277/131
		0−80%	0.409 ± 0.006	124 ± 2	65/128
Au+Au	19.6 (all)	0−5%	0.421 ± 0.003	126 ± 1	293/188
		5−10%	0.414 ± 0.003	128 ± 1	283/184
		10−20%	0.404 ± 0.003	131 ± 1	279/184
		20−30%	0.382 ± 0.003	137 ± 1	322/184
		30−40%	0.363 ± 0.004	138 ± 1	394/185
		40−60%	0.330 ± 0.004	142 ± 1	550/183
		60−80%	0.269 ± 0.006	146 ± 2	644/171

TABLE XII. Same as Table XI, but for $\sqrt{s_{\rm NN}} = 27$, 39, 62.4, and 200 GeV.

System	$\sqrt{s_{\rm NN}}$ (GeV)	Centrality	$\langle\beta\rangle$	T (MeV)	χ^2/nDoF
Au+Au	27 (π, K, p)	0−5%	0.456 ± 0.005	116 ± 2	87/140
		5−10%	0.448 ± 0.005	118 ± 2	73/141
		10−20%	0.434 ± 0.005	122 ± 2	73/141
		20−30%	0.415 ± 0.006	127 ± 2	86/141
		30−40%	0.387 ± 0.007	133 ± 2	105/141
		40−50%	0.354 ± 0.007	139 ± 2	145/141
		50−60%	0.314 ± 0.008	146 ± 2	201/141
		60−70%	0.274 ± 0.009	150 ± 2	283/141
		70−80%	0.23 ± 0.01	153 ± 2	366/139
		0−80%	0.422 ± 0.006	125 ± 2	73/138
Au+Au	27 (all)	0−5%	0.434 ± 0.003	125 ± 1	351/181
		5−10%	0.426 ± 0.003	128 ± 1	302/182
		10−20%	0.414 ± 0.003	132 ± 1	291/182
		20−30%	0.394 ± 0.003	139 ± 1	329/182
		30−40%	0.372 ± 0.004	143 ± 1	365/182
		40−60%	0.337 ± 0.004	149 ± 1	546/182
		60−80%	0.283 ± 0.005	152 ± 2	812/180
Au+Au	39 (π, K, p)	0−5%	0.468 ± 0.005	117 ± 2	58/141
		5−10%	0.449 ± 0.005	123 ± 2	63/141
		10−20%	0.446 ± 0.005	124 ± 2	65/141
		20−30%	0.425 ± 0.006	129 ± 2	98/141
		30−40%	0.395 ± 0.007	137 ± 2	111/141
		40−50%	0.372 ± 0.007	140 ± 2	162/141
		50−60%	0.330 ± 0.008	147 ± 2	235/141
		60−70%	0.292 ± 0.009	155 ± 2	339/141
		70−80%	0.254 ± 0.009	159 ± 2	434/141
		0−80%	0.430 ± 0.006	128 ± 2	70/141
Au+Au	39 (all)	0−5%[a]	0.454 ± 0.004	123 ± 2	132/182
		5−10%[a]	0.442 ± 0.004	127 ± 2	134/182
		10−20%	0.431 ± 0.004	132 ± 2	211/192
		20−30%[a]	0.413 ± 0.004	137 ± 2	264/182
		30−40%[a]	0.392 ± 0.004	143 ± 2	312/182
		40−60%	0.355 ± 0.005	151 ± 2	632/192
		60−80%[a]	0.296 ± 0.006	159 ± 2	879/182
Au+Au	62.4 (π, K, p)	0−10%	0.474 ± 0.006	125 ± 3	105/66
		10−20%	0.462 ± 0.007	129 ± 3	102/66
		20−40%	0.444 ± 0.008	135 ± 3	109/66
		40−80%	0.39 ± 0.01	148 ± 4	193/66
Au+Au	62.4 (all)	0−20%	0.445 ± 0.005	138 ± 2	216/134
		20−40%	0.422 ± 0.006	145 ± 3	205/134
		40−80%[a]	0.376 ± 0.008	155 ± 3	270/118
Au+Au	200 (π, K, p)	0−10%[b]	0.506 ± 0.005	125 ± 2	175/80
		10−20%	0.503 ± 0.006	125 ± 2	153/80
		20−40%	0.483 ± 0.006	134 ± 3	281/82
		40−60%	0.456 ± 0.008	141 ± 3	387/82
		60−80%	0.43 ± 0.01	147 ± 4	549/82
Au+Au	200 (all)	0−10%[c]	0.484 ± 0.004	134 ± 2	300/176
		10−20%[d]	0.488 ± 0.004	132 ± 2	297/174
		20−40%	0.467 ± 0.004	140 ± 2	519/178
		40−60%	0.439 ± 0.005	144 ± 2	931/178
		60−80%[e]	0.422 ± 0.007	149 ± 3	621/124

[a]Lack of measurements of π^0 at this centrality class [47].
[b]The measurements of $\pi^{\pm}$, p, and $\bar{p}$ for centrality 0–12% [43] are used as 0–10%.
[c]The measurements of $\pi^{\pm}$, p, and $\bar{p}$ for centrality 0–12% [43] are used as 0–10%. Λ, $\bar{\Lambda}$, Ξ^+, Ξ^-, and Ω for centrality 0–5% [49] are used as 0–10%.
[d]Lack of measurements of Ω at this centrality class [49].
[e]Lack of measurements of Ω [49] and intermediate p_T $K^{\pm}$ [48] at this centrality class.

TABLE XIII. Same as Table XI, but for $\sqrt{s_{\rm NN}} = 2.76$ and 5.02 TeV.

System	$\sqrt{s_{\rm NN}}$ (TeV)	Centrality	$\langle\beta\rangle$	T (MeV)	χ^2/nDoF
Pb+Pb	2.76 (π, K, p)	0−5%	0.602 ± 0.001	99 ± 1	265/214
		5−10%	0.600 ± 0.001	101 ± 1	274/214
		10−20%	0.597 ± 0.002	104 ± 1	266/214
		20−30%	0.590 ± 0.002	108 ± 1	272/214
		30−40%	0.580 ± 0.002	114 ± 1	334/214
		40−50%	0.566 ± 0.002	120 ± 1	472/214
		50−60%	0.549 ± 0.003	127 ± 2	700/214
		60−70%	0.526 ± 0.003	135 ± 2	1039/214
		70−80%	0.505 ± 0.004	142 ± 2	1371/214
		80−90%	0.484 ± 0.005	143 ± 2	1661/214
Pb+Pb	2.76 (all)	0−10%	0.589 ± 0.001	108 ± 1	541/286
		10−20%	0.584 ± 0.001	113 ± 1	519/286
		20−40%	0.569 ± 0.002	122 ± 1	601/286
		40−60%	0.542 ± 0.002	134 ± 1	816/286
		60−80%	0.507 ± 0.003	146 ± 2	1496/284
Pb+Pb	5.02 (π, K, p)	0−5%	0.613 ± 0.001	99 ± 1	334/91
		5−10%	0.613 ± 0.001	100 ± 1	338/91
		10−20%	0.609 ± 0.001	103 ± 1	356/91
		20−30%	0.602 ± 0.001	108 ± 1	336/91
		30−40%	0.593 ± 0.001	114 ± 1	377/91
		40−50%	0.579 ± 0.002	121 ± 1	519/91
		50−60%	0.559 ± 0.002	131 ± 1	830/91
		60−70%	0.545 ± 0.003	132 ± 2	903/91
		70−80%	0.521 ± 0.004	140 ± 2	1215/91
		80−90%	0.502 ± 0.005	140 ± 2	1324/91

[1] E. Schnedermann, J. Sollfrank, and U. W. Heinz, Phys. Rev. C **48**, 2462 (1993).
[2] E. Schnedermann and U. W. Heinz, Phys. Rev. C **50**, 1675 (1994).
[3] B. De, S. Bhattacharyya, G. Sau, and S. K. Biswas, Int. J. Mod. Phys. E **16**, 1687 (2007).
[4] G. Wilk and Z. Wlodarczyk, Eur. Phys. J. A **40**, 299 (2009).
[5] W. M. Alberico, A. Lavagno, and P. Quarati, Eur. Phys. J. C **12**, 499 (2000).
[6] T. Osada and G. Wilk, Phys. Rev. C **77**, 044903 (2008); **78**, 069903(E) (2008).
[7] T. S. Biro and B. Muller, Phys. Lett. B **578**, 78 (2004).
[8] T. Bhattacharyya, J. Cleymans, A. Khuntia, P. Pareek, and R. Sahoo, Eur. Phys. J. A **52**, 30 (2016).
[9] K. Jiang, Y. Zhu, W. Liu, H. Chen, C. Li, L. Ruan, Z. Tang, and Z. Xu, Phys. Rev. C **91**, 024910 (2015).
[10] Z. Tang, Y. Xu, L. Ruan, G. van Buren, F. Wang, and Z. Xu, Phys. Rev. C **79**, 051901(R) (2009).
[11] J. Adams *et al.* (STAR Collaboration), Phys. Rev. C **71**, 064902 (2005).
[12] G. Wilk and Z. Wlodarczyk, Phys. Rev. Lett. **84**, 2770 (2000).
[13] C. Y. Wong, G. Wilk, L. J. L. Cirto, and C. Tsallis, Phys. Rev. D **91**, 114027 (2015).
[14] K. Urmossy, G. G. Barnafoldi, and T. S. Biro, Phys. Lett. B **701**, 111 (2011).
[15] B. Abelev *et al.* (ALICE Collaboration), Phys. Lett. B **720**, 52 (2013).
[16] K. Urmossy, T. S. Biró, G. G. Barnaföldi, and Z. Xu, arXiv:1405.3963.
[17] K. Urmossy, G. G. Barnaföldi, S. Harangozó, T. S. Biró, and Z. Xu, J. Phys.: Conf. Ser. **805**, 012010 (2017).
[18] M. Rybczyński, G. Wilk, and Z. Włodarczyk, EPJ Web Conf. **90**, 01002 (2015).
[19] W. Broniowski and W. Florkowski, Phys. Rev. Lett. **87**, 272302 (2001).
[20] A. Mazeliauskas and V. Vislavicius, Phys. Rev. C **101**, 014910 (2020).
[21] M. M. Aggarwal *et al.* (STAR Collaboration), Phys. Rev. C **84**, 034909 (2011).
[22] B. I. Abelev *et al.* (STAR Collaboration), Phys. Rev. Lett. **97**, 132301 (2006).
[23] S. Acharya *et al.* (ALICE Collaboration), Phys. Rev. C **99**, 024905 (2019).
[24] F. Retiere and M. A. Lisa, Phys. Rev. C **70**, 044907 (2004).
[25] B. I. Abelev *et al.* (STAR Collaboration), Phys. Rev. C **79**, 034909 (2009).
[26] A. Motornenko, V. Vovchenko, C. Greiner, and H. Stoecker, Phys. Rev. C **102**, 024909 (2020).
[27] A. Andronic, Int. J. Mod. Phys. A **29**, 1430047 (2014).
[28] S. Zhang, Y. G. Ma, J. H. Chen, and C. Zhong, Adv. High Energy Phys. **2016**, 9414239 (2016).
[29] L. Adamczyk *et al.* (STAR Collaboration), Phys. Rev. C **96**, 044904 (2017).
[30] B. Abelev *et al.* (ALICE Collaboration), Phys. Rev. Lett. **109**, 252301 (2012).
[31] H. L. Lao, F. H. Liu, and R. A. Lacey, Eur. Phys. J. A **53**, 44 (2017); **53**, 143(E) (2017).
[32] H. L. Lao, F. H. Liu, B. C. Li, and M. Y. Duan, Nucl. Sci. Tech. **29**, 82 (2018).

[33] S. Zhang, Y. G. Ma, J. H. Chen, and C. Zhong, Adv. High Energy Phys. **2015**, 460590 (2015).
[34] S. Das (STAR Collaboration), EPJ Web Conf. **90**, 08007 (2015).
[35] X. Luo, Nucl. Phys. A **956**, 75 (2016).
[36] S. Chatterjee, S. Das, L. Kumar, D. Mishra, B. Mohanty, R. Sahoo, and N. Sharma, Adv. High Energy Phys. **2015**, 349013 (2015).
[37] M. Shao, L. Yi, Z. Tang, H. Chen, C. Li, and Z. Xu, J. Phys. G **37**, 085104 (2010).
[38] Z. Tang *et al.*, Chin. Phys. Lett. **30**, 031201 (2013).
[39] B. I. Abelev *et al.* (STAR Collaboration), Phys. Rev. C **81**, 024911 (2010).
[40] J. Adam *et al.* (STAR Collaboration), Phys. Rev. C **101**, 024905 (2020).
[41] B. I. Abelev *et al.* (STAR Collaboration), Phys. Lett. B **655**, 104 (2007).
[42] J. Adams *et al.* (STAR Collaboration), Phys. Rev. Lett. **92**, 112301 (2004).
[43] B. I. Abelev *et al.* (STAR Collaboration), Phys. Rev. Lett. **97**, 152301 (2006).
[44] J. Adam *et al.* (STAR Collaboration), Phys. Rev. C **102**, 034909 (2020).
[45] M. M. Aggarwal *et al.* (STAR Collaboration), Phys. Rev. C **83**, 024901 (2011).
[46] B. I. Abelev *et al.* (STAR Collaboration), Phys. Rev. C **79**, 064903 (2009).
[47] A. Adare *et al.* (PHENIX Collaboration), Phys. Rev. Lett. **109**, 152301 (2012).
[48] A. Adare *et al.* (PHENIX Collaboration), Phys. Rev. C **88**, 024906 (2013).
[49] J. Adams *et al.* (STAR Collaboration), Phys. Rev. Lett. **98**, 062301 (2007).
[50] B. I. Abelev *et al.* (STAR Collaboration), Phys. Rev. Lett. **99**, 112301 (2007).
[51] B. Abelev *et al.* (ALICE Collaboration), Phys. Rev. C **88**, 044910 (2013).
[52] B. B. Abelev *et al.* (ALICE Collaboration), Phys. Rev. Lett. **111**, 222301 (2013).
[53] B. B. Abelev *et al.* (ALICE Collaboration), Phys. Lett. B **728**, 216 (2014); **734**, 409(E) (2014).
[54] S. Acharya *et al.* (ALICE Collaboration), Phys. Rev. C **101**, 044907 (2020).
[55] J. Adams *et al.* (STAR Collaboration), Nucl. Phys. A **757**, 102 (2005).
[56] H. van Hecke, H. Sorge, and N. Xu, Phys. Rev. Lett. **81**, 5764 (1998).
[57] J. Adams *et al.* (STAR Collaboration), Phys. Rev. Lett. **92**, 182301 (2004).
[58] M. Petrovici and A. Pop, Rom. J. Phys. **57**, 419 (2012)
[59] O. Ristea, A. Jipa, C. Ristea, T. Esanu, M. Calin, A. Barzu, A. Scurtu, and I. Abu-Quoad, J. Phys.: Conf. Ser. **420**, 012041 (2013).
[60] G. Wilk and Z. Wlodarczyk, Phys. Rev. C **79**, 054903 (2009).
[61] D. Kharzeev and K. Tuchin, J. High Energy Phys. 09 (2008) 093.
[62] F. Karsch, D. Kharzeev, and K. Tuchin, Phys. Lett. B **663**, 217 (2008).